



Investigation of upper mantle discontinuity structure beneath the central Pacific using *SS* precursors

Nicholas Schmerr¹ and Edward Garnero¹

Received 30 November 2005; revised 18 April 2006; accepted 9 May 2006; published 17 August 2006.

[1] Using a high-quality broadband seismic data set of precursors to the phase *SS*, we investigate the structure of upper mantle discontinuities beneath the central Pacific including the Hawaiian hot spot. We image structure by stacking over 4000 records into geographic bins, retaining periods down to 5 s. We consider the effects of correcting for four separate tomographic models of mantle heterogeneity, excluding data at distances containing phases that potentially interfere with precursors. We find evidence for peak-to-peak topography of 15–20 km on the 670-km discontinuity and 7–28 km of topography on the 400-km discontinuity. Weak reflections are detected from discontinuities near 220- and 520-km depth. The average transition zone thickness beneath our region is approximately 242 ± 3 km, very similar to previous estimates of the global average. Lateral transition zone thinning and thickening weakly correlate with reduced and increased transition zone shear velocity, respectively, consistent with a thermal origin to topographical variations on the discontinuities within our study region. The transition zone beneath Hawaii and to the east of the Line Island Chain is thinned by up to 20 km in a province spanning nearly 1000 km, suggesting an excess mantle temperature of ~ 200 K. In the oldest crustal regions of our study area (>100 Ma), the 400-km discontinuity is relatively shallow, and the transition zone is relatively thick (250–255 km); a possible explanation for this pattern includes small-scale convection in the upper mantle bringing colder material into the transition zone.

Citation: Schmerr, N., and E. Garnero (2006), Investigation of upper mantle discontinuity structure beneath the central Pacific using *SS* precursors, *J. Geophys. Res.*, *111*, B08305, doi:10.1029/2005JB004197.

1. Introduction

[2] The transition zone (TZ) of the upper mantle is bounded by two major seismic velocity discontinuities at depths of 400 km and 670 km in the Preliminary Reference Earth Model (PREM) model of *Dziewonski and Anderson* [1981], which have been subsequently established at global average depths of approximately 410 km and 660 km [*Shearer*, 1991, 1996; *Flanagan and Shearer*, 1998; *Gu et al.*, 1998]. These discontinuities are generally agreed to be caused by mineralogic phase changes in olivine, corresponding to the α -olivine to wadsleyite transition at the 400-km discontinuity, and ringwoodite to the Mg-perovskite + magnesiowüstite transition at the 670-km discontinuity [*Ringwood*, 1975]. The depth at which mantle phase changes occur is sensitive to both temperature and chemical composition, and thus regions of chemical and thermal heterogeneity should be accompanied by topography on the discontinuities (see reviews by *Bina and Helffrich* [1994], *Stixrude* [1997], *Helffrich* [2000], and *Shearer* [2000]). The α -olivine to wadsleyite phase change is exothermic [e.g., *Katsura and Ito*, 1989], resulting in the

400-km discontinuity occurring at a greater depth in the presence of anomalously high temperatures in the mantle (shallower in a low-temperature anomaly) and the ringwoodite to Mg-perovskite + magnesiowüstite is endothermic [e.g., *Ito and Takahashi*, 1989], resulting in the 670-km discontinuity becoming shallower in the presence of a high-temperature anomaly in the mantle (deeper in a low-temperature anomaly). Given this probable variation in depth, for notation convenience we adopt the terminology of naming each discontinuity by its PREM depth, such as the 400-km discontinuity as the “400” and the 670-km discontinuity as the “670,” even though the actual depth of each discontinuity is expected to vary. The anticorrelated depth behavior of the 400 and 670 makes discontinuity topography and TZ thickness estimates ideal mantle thermometers, and provides a tool for imaging dynamical, and possibly chemical processes in the mantle.

[3] Additional deep discontinuities have also been proposed, such as the 220-km discontinuity [e.g., *Lehmann*, 1961; *Dziewonski and Anderson*, 1981], a discontinuity or several discontinuities at 250–330 km depth called the X discontinuities [e.g., *Revenaugh and Jordan*, 1991b], as well as a 520-km discontinuity [e.g., *Shearer*, 1990]. The 220 is attributed to several different mechanisms; the tectosphere hypothesis of *Jordan* [1975] suggested the 220 is a chemically distinct boundary layer beneath cratons, *Karato* [1992] attributes the 220 to a switch from anisotropy to

¹Department of Geological Sciences, Arizona State University, Tempe, Arizona, USA.

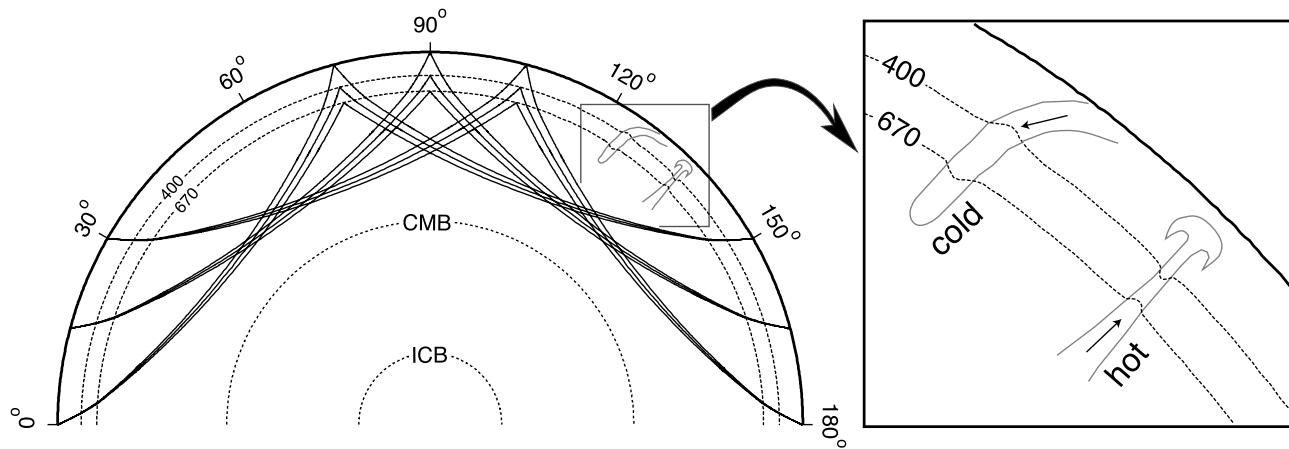


Figure 1. Geometry of *SS* and the precursor phases. The ray paths for three different event/receiver pairs are shown. *SS*, and the precursors occur as underside reflections of seismic energy off discontinuities in the Earth. The precursory phases are most sensitive to structure on the discontinuity at the central bounce point, located halfway between the source and receiver. Also shown are the two major mantle discontinuities at 400 and 670 km depth, as well as the core-mantle boundary (CMB) and inner-outer core boundary (ICB). The cartoon blowup on the right shows the indicated topography induced on each discontinuity from cold or hot material passing into the TZ, e.g., a subducting slab or upwelling plume.

isotropy in the mantle, resulting from a change in the deformation mechanism from dislocation creep to diffusion creep. Seismically, the 220 is only observed regionally, with the most robust observations occurring beneath continents [e.g., Gu *et al.*, 2001; Deuss and Woodhouse, 2002]. The X discontinuities are also attributed to a number of different mechanisms, such as phase changes in the coesite to stishovite SiO_2 systems [Williams and Revenaugh, 2005], the formation of hydrous phase A [Revenaugh and Jordan, 1991b], or a transition from Ca-poor pyroxene to orthoenstatite [e.g., Woodland, 1998]. The X discontinuities are intermittently seismically observed, with sporadic seismic detections beneath continents and oceanic regions using a wide variety of seismic probes (for a review of observations, see Williams and Revenaugh [2005]). The 520 is attributed to the mineralogic phase transformation of wadsleyite to ringwoodite [Ringwood, 1975], though a global seismic study by Deuss and Woodhouse [2001] has suggested multiple 520 discontinuities that may be attributed to phase changes in the garnet system. The 520 has been argued to be a weak global discontinuity [e.g., Shearer, 1991; Flanagan and Shearer, 1998], though in some seismic studies it is only detected beneath continents [e.g., Gu *et al.*, 1998]. Similar to the 400 and 670, the depth, and topography on these additional mantle discontinuities can provide information on the chemical and thermal heterogeneity in the mantle.

[4] A variety of different methods have been employed to image mantle discontinuities, both at regional and global scales (e.g., from several hundreds to thousands of kilometers laterally). The two primary methods are (1) seismic refraction studies of triplicated waves [e.g., Grand and Helmberger, 1984; Ryberg *et al.*, 1998; Song *et al.*, 2004] and (2) secondary phases either converted or reflected at a discontinuity, such as, but not limited to, precursors to *PKPPKP* from underside reflections off discontinuities, *P-*

to-SV conversions at the discontinuity on the receiver side, underside reflections occurring as precursors to *SS* and *PP*, and topside and bottomside reflections of *ScSc* reverberations off the discontinuities (for an extensive review, see Shearer [2000]). In this study, we use secondary phases, precursors to the seismic phase *SS* occurring from underside reflections of upward traveling seismic energy off the bottomside of upper mantle discontinuities (Figure 1). These have been previously used to produce global maps of 400 and 670 topography [e.g., Shearer and Masters, 1992; Shearer, 1993; Gossler and Kind, 1996; Flanagan and Shearer, 1998; Gu *et al.*, 1998; Flanagan and Shearer, 1999; Gu and Dziewonski, 2002; Chambers *et al.*, 2005a]. *SS* and *PP* have also been used to map regional discontinuity topography, for example, with study areas spanning several thousand kilometers [e.g., Lee and Grand, 1996; Niu *et al.*, 2000; Deuss and Woodhouse, 2002; Niu *et al.*, 2002; Rost and Weber, 2002]. The *SS* precursory phase is denoted *SdS*, where *d* is the depth of the underside reflection location beneath the *SS* central bounce point (halfway between source and receiver). *SS* precursors studies have established the 400 and 670 as worldwide features, though using relatively long-period energy (periods > 25 s), providing maps with lateral resolution on the order of several thousands of kilometers [e.g., Flanagan and Shearer, 1998; Gu *et al.*, 1998].

[5] The precursor phases have amplitudes that are typically $\sim 5\text{--}10\%$ (or less) of the amplitude of the reference *SS* phase, which nearly always requires stacking of data to bring the precursor signal confidently out of the background noise. This requires large data sets of records (thousands to tens of thousands of seismograms), which are typically organized into “bins” for stacking by combining data that share similar geographical locations of *SS* bounce points. The ability to accurately measure arrival times of precursors in each bin is dependent on the quality and quantity of data

available for that geographical area. As seismic station networks expand and more earthquakes are recorded, the density of *SS* bounce point sampling has dramatically increased over previous precursor data sets. This improved coverage increases reliability of discontinuity topography estimates for previously undersampled geographic bins, and also allows the *SS* precursor technique to be applied on a more localized scale to specific geographical targets.

[6] A significant challenge is present for *SS* precursor studies aiming to resolve discontinuity topography at regional scales. The minimum-maximum traveltime nature of the *SS* phase [Choy and Richards, 1975] gives rise to a Fresnel zone structure on the order of several thousand kilometers, a dimension that is strongly dependent on the dominant period in the data. Additionally, large amplitude, regional topography on the discontinuities may scatter and defocus the precursory arrivals [e.g., Neele and Snieder, 1992]. The effect of the *SS* precursor Fresnel zone and small-scale scattering on the measurement of discontinuity topography has been the focus of several investigations. Experiments of three-dimensional (3-D) waveform synthesis for models containing discontinuity topography conclude that scattering of energy from high-amplitude, narrow topographic features can potentially bias the stacking of long-period *SS* precursors, resulting in very localized features being smeared over thousands of kilometers [Chaljub and Tarantola, 1997; Neele et al., 1997; Neele and de Regt, 1999]. However, in experiments using Kirchoff synthetics to test stacking resolution of topographic heterogeneity, [Shearer et al., 1999] show that any bias from narrow, small-scale topographic heterogeneity is essentially unresolved by the 10–20° size of the long-period *SS* Fresnel zone. These studies reveal that either scattering and defocusing of precursor energy and/or smearing from relatively large-scale Fresnel zones can result in a potential loss of information about the absolute amplitudes of topography. It is difficult to account for these effects in stacking techniques, which likely result in a smoothing and/or underestimation of discontinuity topography. The consideration of finite frequency effects may provide a future potential tool for unraveling topographic heterogeneity, scattering, and Fresnel zone effects [e.g., Dahlen et al., 2000; Hung et al., 2000]. The unifying limitation of all the previous modeling investigations of *SS* precursors is the restriction to longer periods, and the suggestion that smaller-scale features should become resolved at shorter dominant periods. We are thus motivated to conduct a study of a densely sampled region, to consider the dependency of *SS* precursor analyses on dominant period, and how this possible dependency may map into inferred structure on the discontinuities.

[7] To achieve this, we map TZ structure beneath a region of the central Pacific that is densely sampled by *SS* precursors from a variety of source-receiver geometries. We also search for additional reflectors under this study region. Previous *SS* precursor studies included this region as part of larger global data sets and employed long-period data (~15–25 s dominant period) to map TZ structure [e.g., Gossler and Kind, 1996; Flanagan and Shearer, 1998; Gu et al., 1998; Deuss and Woodhouse, 2002; Gu and Dziewonski, 2002]. Here, we make use of an expansive broadband data set, which enables use of seismic periods as short as 5 s. We investigate the dependence of resultant TZ

topography on seismic frequency, and sensitivity of our results to corrections for upper mantle heterogeneity and overlying crustal structure. Finally, we present maps of discontinuity structure beneath the central Pacific.

2. Central Pacific Study Region

[8] The central Pacific is characterized by a number of features that span several scale lengths (from several hundred kilometers to thousands of kilometers) that make it a valuable target for a regional investigation of TZ structure. Our study spans the region from 0° to 40°N and 135° to 175°W, encompassing two volcanic island chains, Hawaii and Kiritimati (Christmas Island), as well the Hawaiian Seamount Chain, the Line Islands, and the Mid-Pacific Mountains (Figure 2). The crustal age in this region ranges from ~30–120 Ma and crustal thickness is fairly uniform, with a median thickness of 6.9 km, increasing to 15 km beneath the Hawaiian Islands and the Line Islands [Bassin et al., 2000].

[9] The Hawaiian hot spot is a prominent feature in our study area, which has the highest flux rate of erupted material of all known hot spots on Earth [e.g., Sleep, 1990; Steinberger, 2000]. The Hawaiian hot spot has been the target of a number of seismic [e.g., Li et al., 2000, 2004], gravity and geoid [e.g., Cserepes et al., 2000], geodynamical [e.g., Richards and Lithgow-Bertelloni, 1996; Moore et al., 1998], and geochemical [e.g., Ribe, 1988; Liu and Chase, 1991] investigations, as it is hypothesized that an underlying mantle plume feeds the hot spot, which may extend to the core-mantle boundary [Morgan, 1972]. Evidence for a continuous plume throughout the mantle is supported by geodynamical modeling [e.g., Richards and Lithgow-Bertelloni, 1996; Zhong and Watts, 2002], geochemical evidence [e.g., Hilton et al., 1997; Lassiter and Hauri, 1998], and more recently, by seismic tomography [Montelli et al., 2004; Lei and Zhao, 2006]. Recently, a vigorous debate has arisen over the existence of continuous mantle plumes (for a review, see Anderson [2005]), and the topography of the 400 and 670 is an essential constraint in determining if a hot thermal anomaly passes through the TZ beneath Hawaii. Receiver function studies [Chevrot et al., 1999; Li et al., 2000] of the TZ thickness beneath the Hawaiian hot spot have indicated a thinning of ~20–30 km underneath the Big Island of Hawaii, consistent with hot material moving across the TZ and supporting the plume hypothesis. Receiver function studies provide a lateral resolution on the order of several hundred kilometers, but at present are limited in spatial coverage due primarily to the restriction of seismic stations to islands; future deployments of ocean bottom seismometers will extend the receiver function coverage. A seismic phase with a more extended lateral coverage of the central Pacific, such as *SS*, is thus ideal for investigating TZ structure in a vaster region that includes the mantle underlying the Hawaiian chain.

3. *SS* Data Set

3.1. Overview

[10] To investigate the TZ structure beneath the central Pacific, we have collected data with *SS* bounce points that

fall within a 20° radius of the Hawaiian hot spot (19.4°N , -155.3°W , see Figure 2). We also restrict event depths to <75 km to limit the interference of depth phases of earlier arriving phases with the precursory wavefield (e.g. sS_{diff}), and source magnitude $>5.8 M_w$ to ensure good signal-to-

noise ratio (SNR) for the SS phase. The SS precursors are best observed at source/receiver distances $\geq 100^\circ$ to avoid interference with topside reflections off the discontinuities that follow or precede direct S , such as $Ss670s$ and $Ss400s$, and at distances $\leq 165^\circ$ to avoid interference with $ScSScS$ precursors, which, similar to SS , have underside discontinuity reflections halfway between source and receiver. Approximately 1250 earthquakes from around the Pacific recorded by broadband seismic stations with sample rates ≥ 20 Hz in a number of networks in North America and Asia met our criteria for source depth, source magnitude, and distance range, with a total of 4500 seismograms collected from several data centers (Table 1). These records provide a dense sampling of the region surrounding and including Hawaii over a range of azimuths (Figure 2b).

3.2. Basic Data Processing

[11] Before stacking, the broadband data set was processed in the following fashion. The instrument response was deconvolved from each seismogram to obtain displacement, and the horizontal components were rotated to the great circle path. For this study, we used the SH component of motion only. Data were then filtered with a Butterworth band-pass filter with corners at 1 and 100 s, and resampled to 20 Hz, if necessary. Each seismogram was then inspected visually to eliminate records with incomplete time series, remove duplicate seismograms, or check for multiple overlapping events in the precursor and SS time window. Records lacking a clear SS arrival near the PREM-predicted time were discarded. SS arrivals were all unified to positive polarity, and the maximum positive amplitude of SS was picked within a time window defined by the PREM time ± 25 s; this SS peak time is used as a reference time for all subsequent data record alignment (Figure 3). To investigate the possibility of frequency dependence of precursor behavior, the data set was filtered with five different low-pass filter corners: 5, 10, 15, 20, and 25 s. A SNR value was then measured by computing the envelope of each seismogram, windowing 25 s around the enveloped SS pulse, finding the maximum amplitude of energy in that window, and then comparing this to the maximum amplitude of enveloped energy arriving in a time window spanning the precursory wavefield. This time window starts at 25 s before the

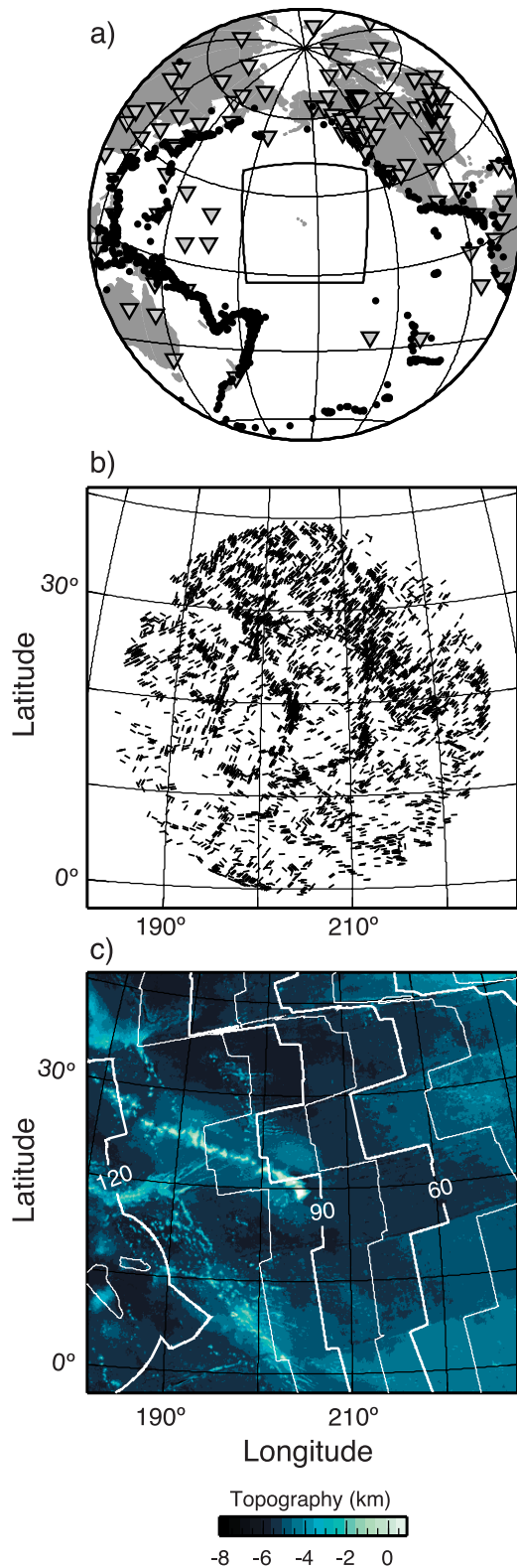


Figure 2. Maps of our study region characteristics. (a) Location of seismic stations (inverted triangles) and earthquake epicenters (solid black circles). The study region is outlined in the central Pacific. (b) Bounce point coverage in the study region, with the event/station azimuth plotted at the location of the geometric bounce point for each seismic record. Coverage is somewhat nonuniform, and we extended our data collection out to 20° from the location of the Hawaiian hot spot (19.4°N , -155.3°W). (c) Bathymetry from ETOPO2.0, available at <http://www.ngdc.noaa.gov/> showing the major geographic features in the study region. Oceanic isochrons (white lines) are shown with a contour interval of 15 million years [Müller *et al.*, 1997]. As with crustal thickness, the ocean depth in our region is also fairly uniform, with a median value of -5100 m.

Table 1. Data Sources

Network	Network Code	Data Source	Number of Records
Chinese Digital Seismic Network (CDSN)	CD	IRIS ^a	4
Canadian National Seismic Network (CNSN)	CN	CNSN ^b	1939
Digital World-Wide Standardized Seismography Network (DWSSN)	DW	IRIS ^a	1
GEOSCOPE	G	GEOSCOPE ^c	270
GEOForschungsNetz (GEOFON)	GE	GEOFON ^d	73
Global Telemetered Southern Hemisphere Network	GT	IRIS ^a	4
Incorporated Research Institutions for Seismology (IRIS) CDSN	IC	IRIS ^a	63
IRIS/International Deployment of Accelerometers (IDA) Network	II	IRIS ^a	545
IRIS/U.S. Geological Survey (USGS) Network	IU	IRIS ^a	1544
Poseidon/Pacific -21	PS	IRIS ^a	99
Terrascope	TS	IRIS ^a	42

^aSee <http://www.iris.edu>.

^bSee <http://www.pgc.nrcan.gc.ca/seismo/seismos/seis-net.htm>.

^cSee <http://geosp6.ipgp.jussieu.fr/>.

^dSee http://www.gfz-potsdam.de/geofon/new/ge_inf.html.

predicted PREM arrival time of the 670 and ends at 25 s following the predicted arrival time of the 220 precursory phase (Figure 3).

3.3. Earthquake Source Normalization

[12] Earthquake source mechanisms of our data range from subduction zone thrust earthquakes to transform faulting at the mid-ocean ridges. It is necessary to consistently identify the arrival of the *SS* reference pulse such that records with different source mechanisms can be stacked in a consistent manner. The *SS* pulse can be further complicated by crustal precursors and postcursors that arrive shortly before and after the *SS* energy [Shearer, 1996]. Even though we limit event depths to ≤ 75 km, the *sSS* depth phase can still complicate identification of *SS* since its amplitude can be similar if not greater than *SS*. The combination of these factors can make identification of the polarity and traveltimes of *SS* less confident, resulting in greater likelihood of blurred or deconstructive stacking of the *SS* precursors we seek to study. Therefore, to equalize the sources in our data set, we experimented with several different approaches, including deconvolution of a reference pulse, varying SNR requirements, low-pass filtering, cross-correlating with synthetic seismograms, as well as a careful visual inspection of each seismogram across records for a given earthquake, including inspecting all records at each station. In the station profiles, contributions to *SS* waveform variability include source mechanism, polarity, and depth phases, but recordings share the same local crustal structure, making this our preferred method for selecting the *SS* arrival and polarity. We also generate a reflectivity synthetic seismogram [Fuchs and Müller, 1971; Müller, 1985] for every observed seismogram, using the appropriate moment tensor solution when available, event depth, distance, source azimuth, and the PREM model. Our PREM synthetic seismograms serve as a control in our experiments with the *SS* wavefield. Example reflectivity synthetics are given in Figure 4, for two different source depths. In the absence of noise, the underside and topside discontinuity precursors, as well as depth phases, are all easily visible. Each synthetic record is then filtered using a Butterworth low-pass filter with corners at 5, 10, 15, 20, and 25 s. After filtering, the peak amplitude of the synthetic *SS* pulse is reselected to

account for any smoothing and shifting of the peak in the filtered trace.

4. Stacking Method

4.1. Slowness Stacking Procedure

[13] All stacking methods have the goal of increasing the signal of the phases of interest while reducing the amplitude of incoherent noise. Here, we stack on specific slownesses (or moveouts), which results in constructive interference for coherent energy in the stacked traces present at the stacking slowness, and destructive interference for all other energy. This stacking method is similar to that used in previous *SS*

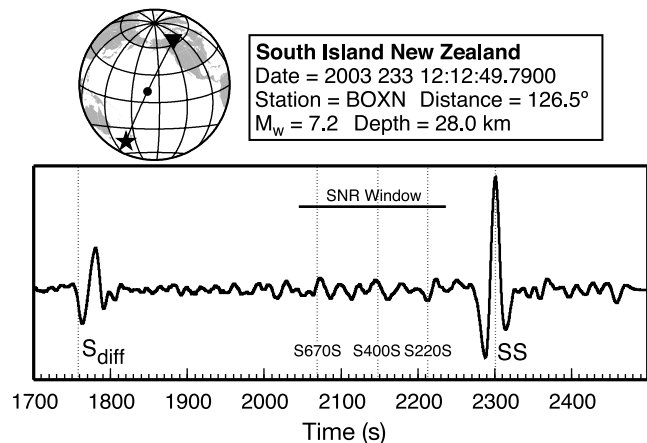


Figure 3. An example of a high-quality broadband SH component displacement seismogram. This seismogram was collected from the CNSN, with the earthquake (star) and receiver location (inverted triangle) shown on the small globe in the top left. The bounce point of the *SS* phase is shown by the black circle. The predicted PREM arrival times for *S_{diff}*, *S670S*, *S400S*, *S220S*, and *SS* are plotted as dotted vertical lines. The signal-to-noise ratio is measured by finding the maximum enveloped amplitude in a time window extending from ~ 25 s preceding *S670S* to ~ 25 s after the *S220S* arrival time and comparing this to the maximum amplitude of the *SS* arrival.

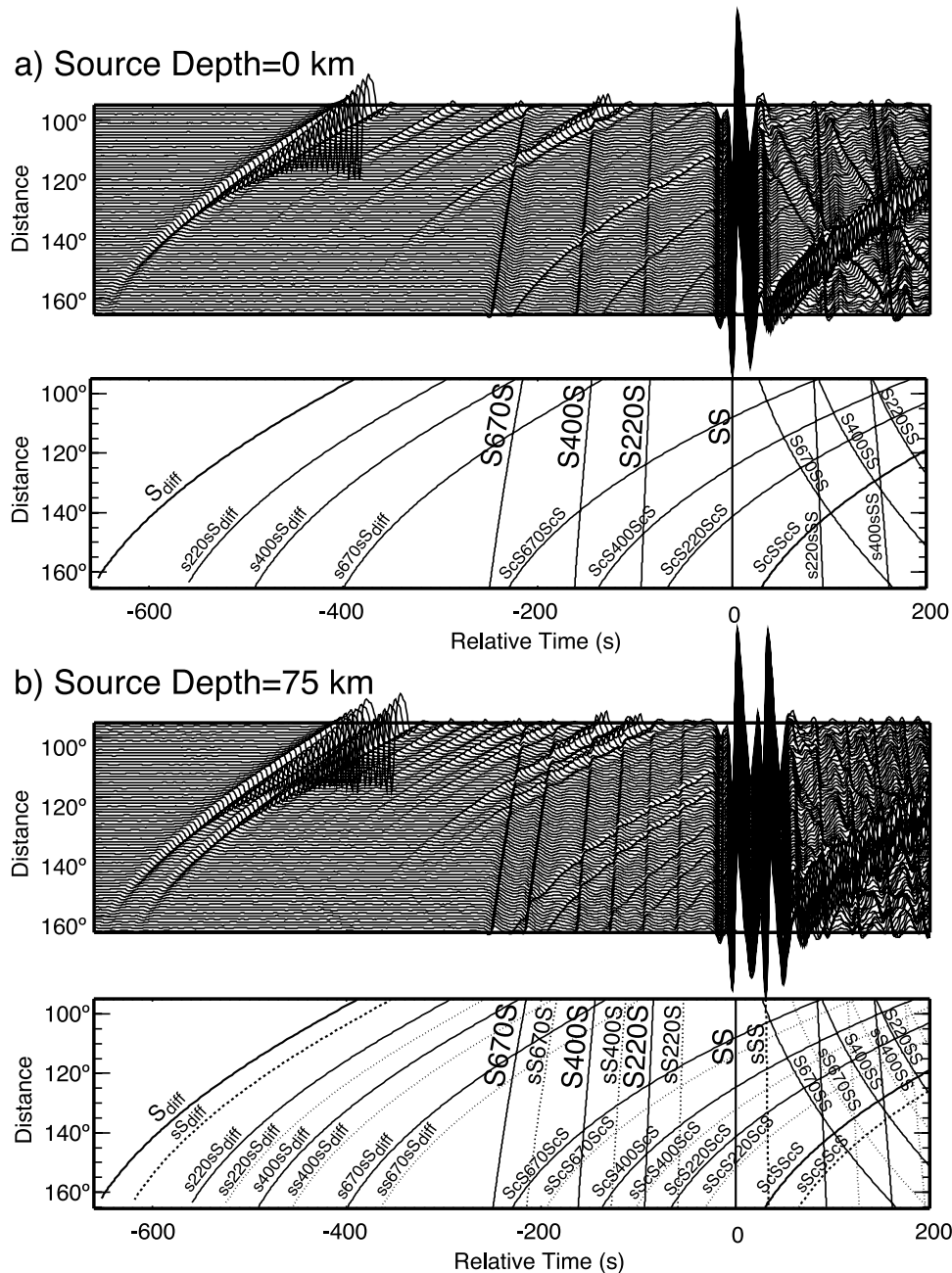


Figure 4. SS wavefield from reflectivity SH component displacement synthetics for two different source depths: (a) 0 km and (b) 75 km. Below each panel, the expected PREM traveltimes for direct phases (solid lines) and depth phases (dotted lines) are labeled. Times are relative to the SS arrival, which is assigned to zero, and amplitudes are normalized to the maximum positive amplitude of the SS pulse. The precursors are obscured at particular distances because of constructive/deconstructive interference with other seismic phases, as well as depth phases. At shorter distances (100–120°) this is especially pronounced, illustrating the need to exclude certain distances for different precursors to avoid biasing discontinuity depths in stacking.

studies [see Flanagan and Shearer, 1998; Gu et al., 1998] and is as follows:

[14] 1. The maximum amplitude of SS in each record is normalized to unity to equalize the energy across a variety of source mechanisms and radiation patterns. The timing of this peak is defined with a reference time of zero.

[15] 2. For each seismogram, the predicted differential traveltime between SS and the SdS precursor of interest is computed to correct for the different moveout of SS precursors to SS through epicentral distance. At any specific distance (Δ), we note this differential time as $T_{SS-SdS}^{pred}(\Delta)$; this time increases with distance, following a curved traveltime

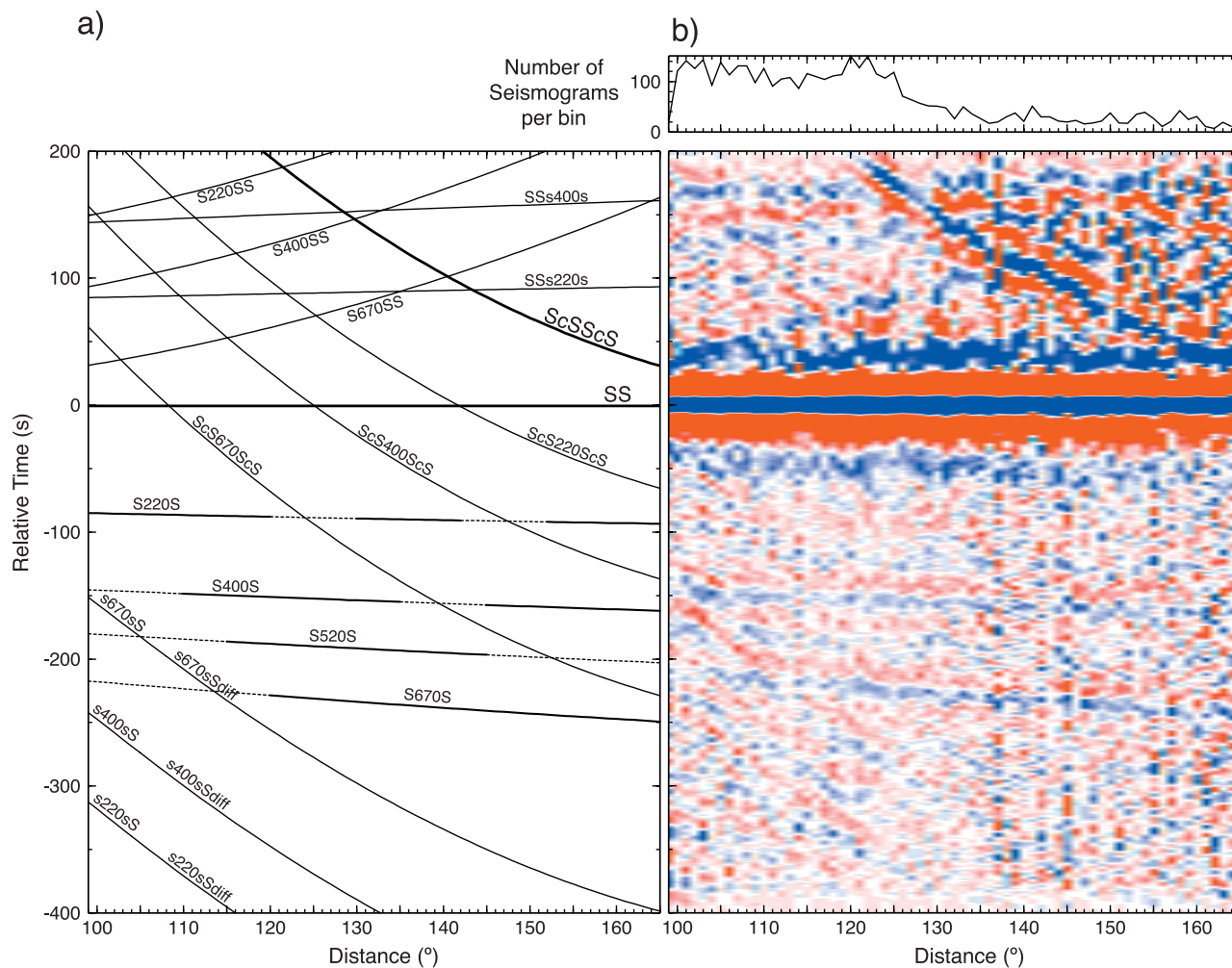


Figure 5. Predicted traveltimes plot for the *SS* wavefield and distance stacks for all data. (a) PREM predicted traveltimes for *SS* wavefield. The source is at the surface, and the traveltimes for a hypothetical 520 is also shown. Thin dotted lines indicate distance ranges that are excluded in the geographic stacking to prevent interference from nonprecursory phases, such as depth phases (not shown), topside reflections, and precursors to *ScSScS*. (b) The 1° epicentral distance bin stacks for the entire data set at 10-s dominant period, illustrating the energy present in the data set. Records are binned in 1.0° distance increments and stacked on the *SS* peak amplitude. Blue represent positive amplitudes and red is negative; both colors are made to saturate at approximately $\pm 10\%$ the maximum amplitude of *SS* to bring out low-amplitude phases. At the top, is a histogram of the number of records for each stack. *SS* and *ScSScS* are the largest amplitude arrivals, and energy can be seen for *SS* precursors (*S400S*, *S670S*), topside reflections (*s400sS*, *s670sS*), and for *SSS* precursors (*S670SS*), as well as *SSs400s*, and weak *ScSScS* precursor energy.

trajectory (e.g., Figure 4) which varies for different *SdS* reflector depths d . To coherently stack records across a range of distances, an arbitrary reference distance (Δ_{ref}) is selected for time alignment of the records, here, 125° . Therefore each record is then shifted by the quantity $T_{SS-SdS}^{\text{pred}}(\Delta_{\text{ref}}) - T_{SS-SdS}^{\text{pred}}(\Delta)$ to align the precursor of interest before seismogram summation. This time shift is zero at the reference distance, positive at distances less than Δ_{ref} , and negative at distances greater than Δ_{ref} .

[16] 3. Records at distances with predicted interference between precursors of interest and other phases are omitted from the stack, as interfering phases can bias the stack if present in a particularly well-sampled distance window (Figure 4). For example, the 670 precursor *S670S* is

contaminated by energy from *s670sS* at distances between $\sim 100^\circ$ to 120° , causing a potential contamination of a stack biased at these distances (e.g., Figure 4, see also Figure 5).

[17] 4. A stacking weight is determined for each record based on its *SS/SdS* SNR value. This step is aimed at equalizing the energy between records with differing amounts of background noise, and/or a weak *SS* pulse. As the precursors are predicted to have amplitudes on the order of 10% of the *SS* amplitude, an ideal precursor window will have relatively low amplitudes relative to *SS*, therefore a high SNR, and is given greater weight in the stack. Records with a high level of noise, *SS* near a nodal azimuth in the earthquake radiation pattern, or other interfering phases in

the precursor wavefield, will tend to have low SNR values, and therefore have a lesser weight in the stack.

[18] 5. Timing corrections (shifts) are applied to each record for estimations of timing perturbations due to mantle heterogeneity, crustal thickness variations, and surface topography (detailed in section 4.2), each of which can affect the differential time between *SS* and precursors.

[19] 6. The record section is then summed to produce a stack. A bootstrap resampling technique with 100 random resamples is used to estimate the 95% confidence level for the energy in each stack [e.g., see *Efron and Tibshirani*, 1986].

[20] 7. Precursor timing is then measured if its peak amplitude in the stack has formed reasonably near its expected arrival time, and if it has amplitude above the 95% confidence level from the bootstrap. The timing of the pulse is measured by picking the peak amplitude of the precursor pulse using the bootstrap boundaries (see section 4.4). The time pick from the stack can then be converted to discontinuity depth by comparison to time predictions of perturbed discontinuity depths in the PREM model. Figure 5 shows the results of stacking the entire data set by epicentral distance on the *SS* phase, where many additional arrivals are readily apparent.

[21] This procedure is similarly applied to both data and PREM reflectivity synthetics. The synthetics provide an additional constraint on the accuracy of our method, as their precursor phases arise from discontinuities with known depths (400 km and 670 km), and thus will reveal any biases in the stacking procedure (such as those that may arise from interference with depth phases).

4.2. Prestack Timing Corrections

[22] The timing of the peak amplitude of the *SS* arrival is first adjusted to account for the traveltime delay accrued from variation in crustal thickness and surface topography. This is done for each record; we use CRUST2.0 [*Bassin et al.*, 2000] to construct a crustal velocity and thickness model at the geometric *SS* bounce point. Zero depth is taken as mean sea level, and each crustal model is adjusted for surface topography/bathymetry (see Figure 2). The *SS* ray parameter is used to ray trace through PREM with the modified crust to compute the crustal and topography traveltime correction for each record (Figure 6a).

[23] We also apply a time adjustment for perturbation from lateral heterogeneity using 1-D ray tracing through several different tomographic models [*Li and Romanowicz*, 1996; *Ritsema et al.*, 1999; *Masters et al.*, 2000; *Grand*, 2002] (Figure 7). This differs from previous efforts that used an average correction computed for each data stack rather than correcting each prestack record independently [e.g., *Flanagan and Shearer*, 1998] but is similar to that of *Gu et al.* [1998], *Gu et al.* [2001], and *Gu and Dziewonski* [2002], who apply an average correction computed for each bin prior to stacking. We find mean tomographic correction values for the prestack method are very similar to those for a poststack correction, indicating the two methods should produce comparable results. However, in our method, the prestack correction is easier to implement as heterogeneity only has to be calculated once for each seismogram and reflector, rather than for each stack independently. The tomographic correction is computed for each record by

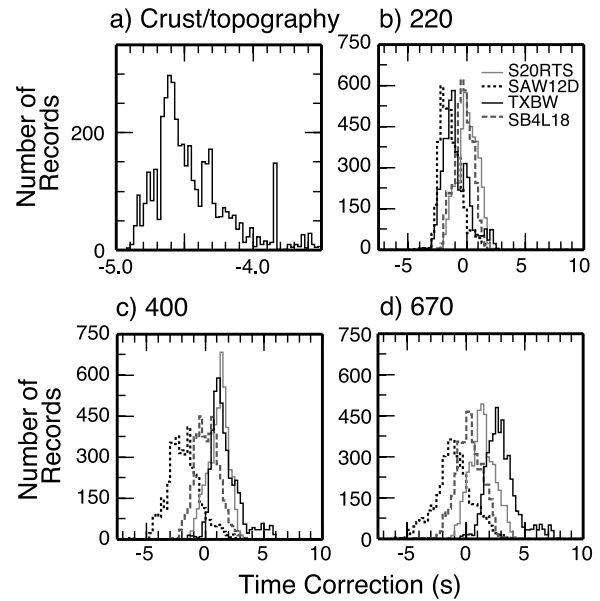


Figure 6. Histograms of the corrections used for stacking, showing the spread of values across all records. (a) Total correction for crustal thickness and topography, the correction is relative to PREM (with no ocean), so negative values indicate early arrival of *SS* due to a thinner crust and/or lower topography relative to mean sea level. (b–d) Tomographic corrections for stacking of various discontinuity depths and several tomographic models. The correction is the amount of traveltime anomaly accrued by the *SS* phase along its entire ray path minus the amount of traveltime anomaly accrued along the entire precursory ray path. Negative values indicate a relatively fast path (*SS* arriving early relative to the precursors, or the precursors arriving late relative to *SS*), and positive values indicate a relatively slow path (*SS* arriving late relative to the precursors, or the precursors arriving early relative to *SS*).

separately ray tracing the paths of *SS* and all precursory phases introduced into PREM, which are used to compute traveltime perturbations through the global models. Thus the PREM predicted *SS* and *SdS* traveltimes are subtracted from that predicted due to the tomographic model, to define a traveltime residual prediction:

$$T_{SS-SdS}^{tomo} = (T_{SS}^{PREM} - T_{SS}^{tomo}) - (T_{SdS}^{PREM} - T_{SdS}^{tomo}).$$

This tomography correction is computed separately for each precursor ray path, since they sample different depths through the upper mantle and transition zone (Figures 6b and 6c). This method does not consider the 3-D sensitivity of the *SS* Fresnel zone or 3-D ray tracing effects [e.g., *Hung et al.*, 2000; *Zhao and Chevrot*, 2003]. Experiments investigating the wavefield effects from 3-D small-scale heterogeneity [e.g., *Igel and Gudmundsson*, 1997; *Zhao and Chevrot*, 2003] show strong dependence of traveltimes on the relative degree of heterogeneity of the input tomographic model. However, most tomographically derived models of global heterogeneity are relatively smooth (variations are typically on the order of thousands of kilometers); also, all timing corrections are differential

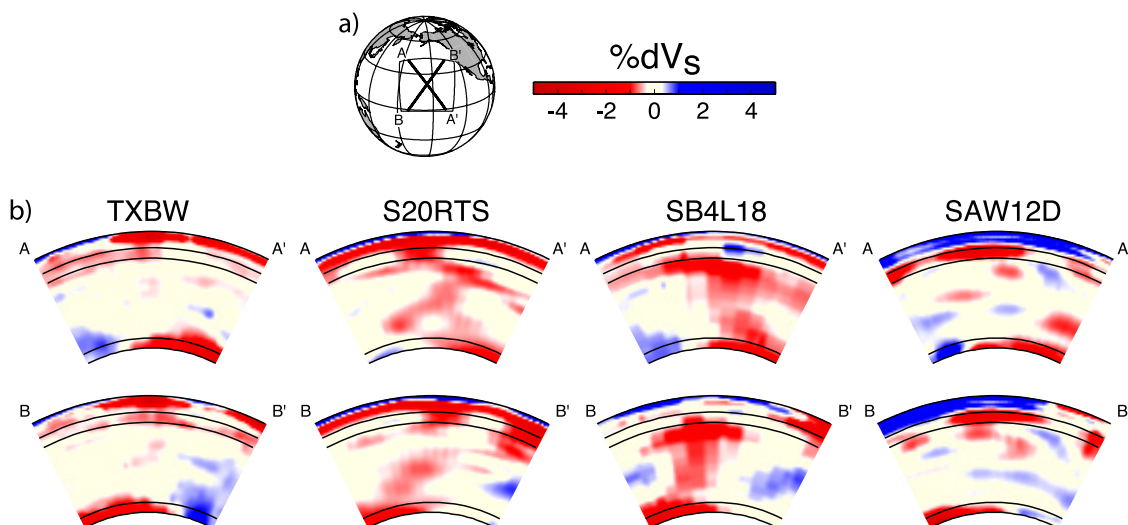


Figure 7. Cross sections through the different tomography models used to correct for mantle heterogeneity in our study. (a) Locations of the cross sections A-A' and B-B'. The study region is outlined by the plotted box. (b) Cross sections through the models. No vertical smoothing is made between layers in the models, and all models are laterally resampled into $2^\circ \times 2^\circ$ elements to facilitate comparison between different parameterization methods (e.g., shells, spherical harmonics). Note that TXBW values are given in reference to a 1-D reference model that differs from PREM, all the other models are relative to PREM. TZ heterogeneity typically does not extend beyond $\pm 1\%$ about the mean value in our region (though the cross section through the SAW12D model shows some anomalies that exceed -2.5%), so we adjust the color scale to saturate above these levels to show maximal variation in the TZ.

between *SS* and the precursors, helping to minimize 3-D effects.

4.3. Stacking Geometries

[24] One stacking experiment is to simply stack the entire data set for a particular precursor into one summary stack to obtain the average discontinuity depth throughout the study region. The data can also be stacked into epicentral distance bins, as is shown in Figure 5. Another method for stacking precursor data is to bin the data into geographic “caps” of a given radius [e.g., Flanagan and Shearer, 1998]. The average location of the bounce points falling within the cap or distance from the cap center [e.g., Gu *et al.*, 2003] can then be used to adjust the cap’s location. If the data sampling density permit analysis over a number of geographic caps, a map of TZ structural variations can be produced.

[25] We adopt the approach of stacking geographically centered caps and explore several permutations upon this method; we vary bin size, the number of bins, and the bin location (Figure 8). Bin size is varied from 5° , 10° , to 20° , and we expect larger bin sizes to average more data together, essentially smoothing structure. The number of bins is varied from 25, 80, to 351, and is designed to test the coherency of structure between neighboring bins, and check the effects of oversampling/undersampling a region with a nonuniform distribution of *SS* bounce points. For the 25-bin geometry, we used equal-distant bins separated by 10° , for the 80 and 351 bins, we used equidistant radial spacing. For each bin, a mean location of the stack is found by averaging all the bounce points that fall within the bin. The mean location better represents the sensitivity of each particular stack to underlying structure than the actual bin center and

is used to plot the resulting topography and transition zone thickness measurements. Therefore the final location of stacks will differ from the starting locations shown in Figure 8.

4.4. Conversion to Discontinuity Depth

[26] The stacks are made for a variety of precursor slownesses, corresponding to *SdS* reflector depths between 150 and 670 km. After stacking, the timing of the precursor of interest is converted to discontinuity depth by interpolating between computed theoretical arrival times for reflectors at different depths embedded in the PREM model at the reference distance (Δ_{ref}). This requires a systematic pick of precursor arrival times. In our initial experiment with stacks of the entire data set, we found the precursor arrival time by picking the peak amplitude of the precursor pulse that arrives closest in time to the predicted peak for that depth. Experiments in cross-correlating the synthetics with the *SS* pulse showed a level of bias away from this peak, mainly attributed to a mismatch in the *SS* and precursor waveforms. This mismatch is a result of *SS* becoming defocused from stacking on a moveout appropriate for the precursor. In the geographical cap stacks, the peak precursor amplitude was also picked, and we experimented with cross-correlating the synthetic precursor pulse with the precursor pulse from the corresponding synthetic stack of the entire data set to better improve arrival time estimates. There was a systematic bias away from the mean precursor pulse for asymmetric or poorly populated precursor stacks, which would invariably increase when stacking the actual data set. We found that arrival time picks in the irregular stacks were more reliable when the 95% confidence boundaries from the bootstrap were used to adjust the peak

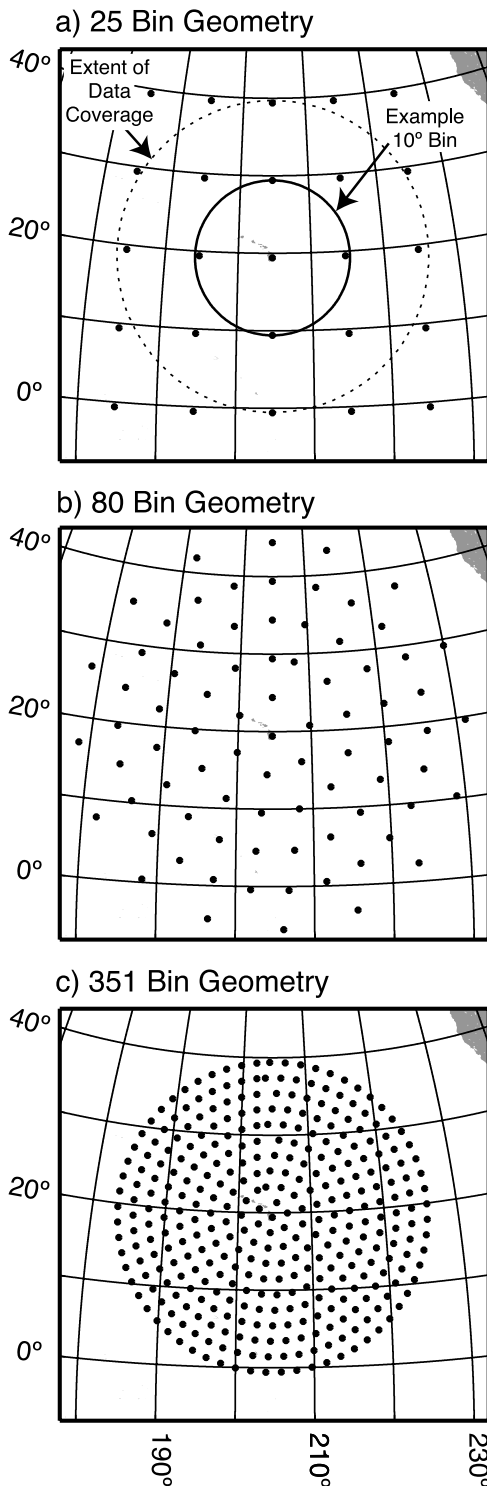


Figure 8. Maps showing bin geometries used in stacking. The central location of each cap is plotted as a black dot. (a) The cap geometry for 25 equally spaced bins, each 10° apart. An example 10° radius bin is shown for the bin centered on the Big Island of Hawaii. The extent of our data set is also shown by the dotted line; we place bins outside this sample area to test the structure at the edges of our study region. The 80 and 351 equidistantly spaced caps: bins approximately (b) 5° apart and (c) 2.5° apart. Note that these are the starting locations and that each bin is relocated on the basis of the bounce points that fall within it (see text).

amplitude. This consists of selecting the peak amplitude as before; the bootstrap boundaries are then used to define a time window about this amplitude in the pulse. We tested this with our synthetic stacks; for asymmetric pulses, the arrival time picked for the precursor from simply selecting the peak amplitude is skewed from the center of this time window, producing a slight offset in expected precursor timing. For symmetric pulses, the arrival time picked falls at the mean time within the bootstrap window, and very near the predicted arrival time for the precursor. We therefore adjust our time picks for precursor delay times in the data stacks to fall at the mean time within this 95% confidence time window. Finally, these delay times are mapped to discontinuity topography by interpolating between our theoretical delay times for different precursor depths.

5. Results

5.1. Stacking Experiments

[27] To begin, we stack the entire precursor data set over a variety of slownesses to search for mantle discontinuities and test the effects of the various corrections. We stack at slownesses for discontinuities at depths of 150, 220, 300, 400, 520, and 670 km. Synthetic experiments show that an error of $\pm 1-2$ km in depth estimate arises from stacking along a moveout corresponding to a discontinuity displaced by up to ± 20 km. Stacks for the entire data set, using the distance exclusions outlined in Figure 5 and Table 2, are shown in Figure 9. Only *S400S* and *S670S* appear to stack coherently across the central Pacific study region. The negative swing following these two precursors is depth phase energy (*sS400S* and *sS670S*). There is a very weak reflector, barely above the 95% confidence level at 520, and another corresponding to a depth just above the 220 riding the long-period down swing preceding *SS*, though both scarcely fall above bootstrap boundaries. Other reflectors at ~ 320 - and 280 -km depth can be found in a limited number of geographic stacks, but not in stacks of the whole data set. The distance exclusion preprocessing step described in section 4.1 is crucial for minimizing stacking error from interfering phases, as these low-amplitude phases can be obscured by interfering phases. This is best illustrated by *S520S*, where the distance ranges $100-115^\circ$ and $145-165^\circ$ are excluded. Data at these distance ranges are interfered with by *s670sS* and *ScS670ScS* (Table 2) near or around the *S520S* arrival time. Stacking with these distance ranges included produces a higher-amplitude pulse near the *S520S* arrival time, which could be mistaken for reflected energy from the 520-km discontinuity. Discontinuity depth estimations can be significantly skewed, even for higher-amplitude precursors (e.g., *S400S*, *S670S*), when including distance ranges of interfering arrivals. For example, the 670 can be offset by 5 km or more from interference with *s670sS* and its associated depth phase. This behavior is independent of SNR, tomography model, and dominant period.

[28] Stacks of the entire data set over a range of SNR and dominant periods were also made to study the effects of these variables on the inferred discontinuity depth. Stacks were computed for each SNR range: ≥ 0.0 (entire data set), ≥ 1 , through ≥ 6 , with each higher SNR cutoff corresponding to $\sim 10\%$ reduction in the number of data in

Table 2. Distance Exclusions

Discontinuity Depth, km	Distances Excluded	Potentially Interfering Phases ^a
150	110–120°	ScS670ScS, sScS670ScS
	130–140°	ScS400ScS, sScS400ScS
220	120–130°	ScS670ScS, sScS670ScS
	142–152°	ScS400ScS, sScS400ScS
300	127–137°	ScS670ScS, sScS670ScS
	150–165°	ScS400ScS, sScS400ScS
400	100–110°	s670sS, ss670sS
	135–145°	ScS670ScS, sScS670ScS
520	100–115°	sS670S, s670sS, ss670sS
	145–165°	ScS670ScS, sScS670ScS
670	100–120°	s400sS, s670sS ss400sS, ss670sS

^aTopside reflections *sdsS* and *ssdsS* transition to *sdsSdiff* and *ssdsSdiff* at $\sim 106^\circ$, for brevity, this is not shown. Depth phases are not shown, but distances are extended to incorporate these arrivals.

each stack. The dominant periods explored were 5, 10, 15, 20, and 25 s. The 15–25 s range is comparable to previous *SS* precursors studies. We also varied the tomography model used to correct for upper mantle heterogeneity. Coherent *SdS* arrivals were found in the slowness stacks corresponding to the 400-, 520-, and 670-km depth discontinuities, though the *S520S* arrival becomes weak and difficult to identify at shorter periods. Altering the SNR cutoff generates depth variations of ± 2 –4 km for the 400 and 670, and by ± 5 km for the 520. This variability can be attributed to the diminishing number of records in each stack for larger SNR cutoffs (Figure 10). An uneven distribution of bounce points could potentially over sample localized topography, resulting in a stack more representative of the over sampled areas than of the entire study region's average. This effect would become more pronounced as the number of records in the stack is decreased and the distribution of bounce points became more uneven. We further explore this later by varying the size of the geographic bins, and hence the size of the region over which we average structure. Our data set exhibits geographic clustering of *SS* bounce points (Figure 2b), and increasing the SNR cutoff reduces the density of our regional coverage. The difference between mean depths and TZ thickness for the SNR cutoffs also becomes more pronounced at the shorter periods, as the longer-period data tend to have a larger number of records that fall into the higher-quality SNR cutoffs (Figure 10). Statistically, averaging fewer records together should produce higher peak-to-peak topography measurements, as there are less data to smooth out extremes. Therefore we expect stacks at higher SNR cutoffs to smooth structure less and to show more topography than those with more records.

[29] Another source of variability in discontinuity depth determination comes from choice of tomographic model used to correct for upper mantle heterogeneity. The absolute depth of the 400 varies by ± 4 –5 km, the 670 by ± 5 –7 km, and the 520 by ± 6 –9 km between tomographic models. This absolute depth variation is due to differences in upper mantle heterogeneity between the tomography models and not likely attributable to actual discontinuity depth variation. The differential measurement of TZ thickness minimizes contributions of heterogeneity from upper mantle structure, with the overall mean value changing by ± 2 –

3 km between the models. Differences in upper mantle heterogeneity between tomography models thus maps into different absolute discontinuity depths depending on the tomography model used for correction. Also, depending on the model used, tomographic corrections result in a slightly thicker or thinner TZ, though our average value of ~ 242 km across all models is identical to the global average of ~ 241 –242 km [e.g., *Gu and Dziewonski, 2002*]. This aspect is explored further in geographic bin stacks of the data, allowing the comparison of resultant discontinuity topography across different tomographic models.

[30] To investigate variable discontinuity structure on the 400 and 670 within our overall study region, we bin the data geographically and measure discontinuity depths in each bin to produce a map of lateral variations in discontinuity structure. We also note a regional detection of the 520 but

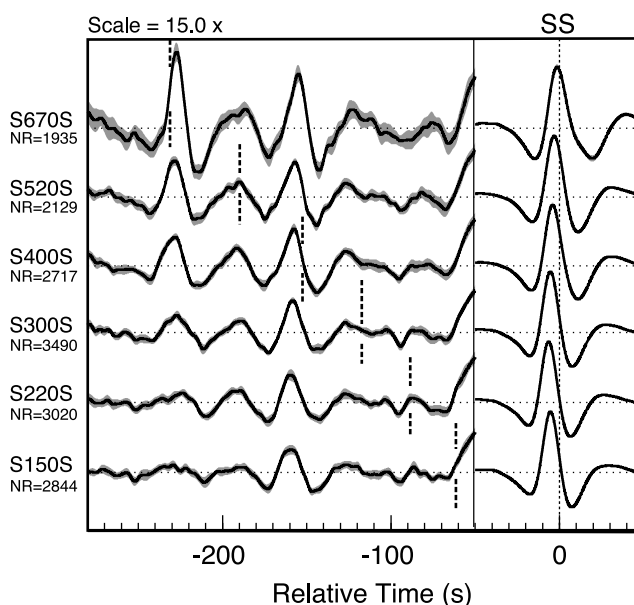


Figure 9. Stacks of the entire data set on different slownesses to search for coherent reflectors at different depths. The dominant period of the data shown here is 10 s, and no SNR exclusion was used. Data were corrected for mantle heterogeneity using the TXBW model. Data traces are shown as solid lines, with the upper and lower boundaries of the 95% confidence level from bootstrap resampling shown as gray shading around the data stack. The precursor wavefield is multiplied by a scale factor (here 15X) to improve visualization of lower-amplitude phases, and each trace is normalized to the maximum amplitude of the *SS* pulse with zero amplitude delineated by the horizontal dotted line. Each trace represents a stack on a particular slowness, with the dotted vertical line marking the expected arrival time for each reflector. The offset in the arrival time of the *SS* pulse is from the corrections for upper mantle heterogeneity as well as crustal corrections and the slightly different moveout of *SS* and the precursor. The number of records in each stack varies due to the exclusion of different distances to limit the interference of other phases (Table 2). Coherent arrivals are seen at slownesses of 400 and 670, and very weak reflectors are seen at 220-km and 520-km depth.

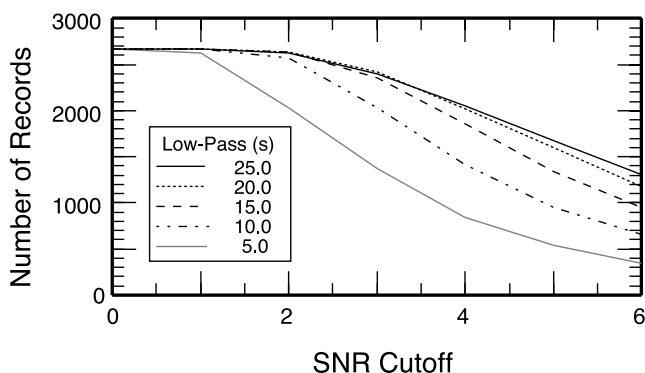


Figure 10. Number of records in stacks of all the data for different SNR cutoffs and low-pass filters of the data set. The number of records shown is for stacks on the 400, with appropriate distance exclusion windows turned on for this depth. In general, though the absolute number of records may change for different slownesses, the pattern of decreasing amounts of records at higher SNR cutoffs remains the same across different filters. Higher-frequency data tend to have larger amounts of noise, leading to a reduction in the number of highest-quality records.

do not explore this feature further as it is only sporadically present in about 25% of our bins and is does not fall above the 95% confidence level in stacks at shorter periods. We do not present stacking results for *S220S*, as very few stacks had significant coherent energy corresponding to this discontinuity.

[31] We perform a number of tests to understand the contributions of stacking method, time shifting corrections, SNR values, and dominant periods of the data set to the resultant discontinuity topography. Figure 11 shows an example of *S400S* and *S670S* stacks, along with resultant discontinuity depth estimations. Depth estimates are bounded by the 95% confidence levels, and only energy falling significantly above these bounds is considered as a robust reflection from the discontinuities; the bootstrap uncertainty boundaries increase at shorter periods and higher SNR cutoffs. More noise is present in the 5-s low-pass data, and fewer records are available for the higher SNR cutoffs, but even at the highest SNR and shortest periods, robust reflections occur from both the 400 and 670.

[32] We stack the data using the different number of bins shown in Figure 8 for 5°, 10°, and 20° sized caps. Stacks that do not form precursory energy above the 95% confidence level are discarded, and not plotted in the subsequent sets of figures. The resulting thickness patterns of the TZ for stacks are virtually identical across the different number of overlapping caps (Figure 12a). The deviation between the three sampling densities lies in the outer most stacks that are near the edge of our data coverage, which are generally underpopulated by *SS* bounce points. The bins lying near or at the study region boundary are almost always excluded due to lack of robust energy for measuring precursor depths. This is purely a result of the cutoff in the extent of our data coverage, and does not represent actual structure. This is especially apparent in the 25-bin geometry, where the southwest, northwest, southeast, and northeast corners are generally underpopulated and excluded from the measured

topography. We therefore selected the 80-bin geometry as our preferred bin geometry as it gives good coverage of our study region, better approximates our data coverage, and does not require an overly large number of stacks for each discontinuity depth, low-pass filter, correction model, and SNR cutoff. The effect of SNR is shown in Figure 12b and demonstrates that for low SNR cutoffs, the thickness retrieved for the TZ is very similar, with peak-to-peak thickness varying from 13 to 24 km. However, at higher SNR cutoffs, TZ peak-to-peak variation in thickness increases to 15–30 km; fewer records are available, but are of higher quality, producing robust stacks that average less structure together. In altering the cap size (Figure 12c), we find that the 20° caps produce TZ thicknesses very similar to the stacks of all the data, with the whole region appearing to be flat. The 5° caps produce similar topography patterns to the 10° caps, and the peak-to-peak amplitude of topography is increased by 5–10 km, comparable to that found in the high SNR cutoff. However, the 5° caps collect about 25% of the bounce points that fall within the 10° caps, causing many stacks to have weak precursory arrivals, as is evidenced by the lack of coverage compared to the 10° and 20° bins. Ideally, we would use the highest-quality data and smaller bin sizes, but in practice these parameters trade off with the number of records in the stacks, reducing the amount of robust stacks that can be used for measuring TZ structure. The cap size acts much like a filter of the resulting topography, but trades off with the number of records in a stack and ultimately the robustness of the stack. Therefore we prefer the 10° cap size, as this bin size nearly always produces robust stacking results.

[33] Stacking results for the TZ thickness variability across different low-pass filters of the data are shown in Figure 13. In general, there does not appear to be any strong dependence on low-pass filter of the data set, though at the shortest-period, 5 s, there is a 2–3 km increase in peak-to-peak topography. However, at this period, a larger number of stacks need to be excluded due to lack of robust precursor energy, suggesting the additional variability may be noise contaminating the topography measurements. The 10-s data appear to be the shortest period at which robust stacks can be retrieved from our data set, though with denser data coverage, utilizing 5-s energy is entirely possible.

[34] As in the stacks of all the data, the largest source of variation between the geographic stacks is the tomographic model used to correct for discontinuity depths. Figure 14 shows topography on the 400 and 670, as well as the TZ thickness for the four different tomography model corrections used in this study. We also investigate the effect of SNR cutoff, as our previous experiments indicate that the higher-quality data produce more topography variation. The tomographic correction adds 5–10 km of relief compared to the uncorrected stacks shown in Figure 13. This increase in heterogeneity is predicted; velocity heterogeneity produces traveltime anomalies that tend to cancel out traveltime anomalies arising from topography on the discontinuities (see section 6.2). Regardless, the topology retrieved is similar to when no tomography correction is applied (compare the TZ thickness in Figure 14a to Figure 13), though some of the small-scale details vary. At a SNR cutoff of 3, there is more relief on the 670 than the 400, with peak-to-peak topography of 6–18 km on the 400 and 15–20 km on

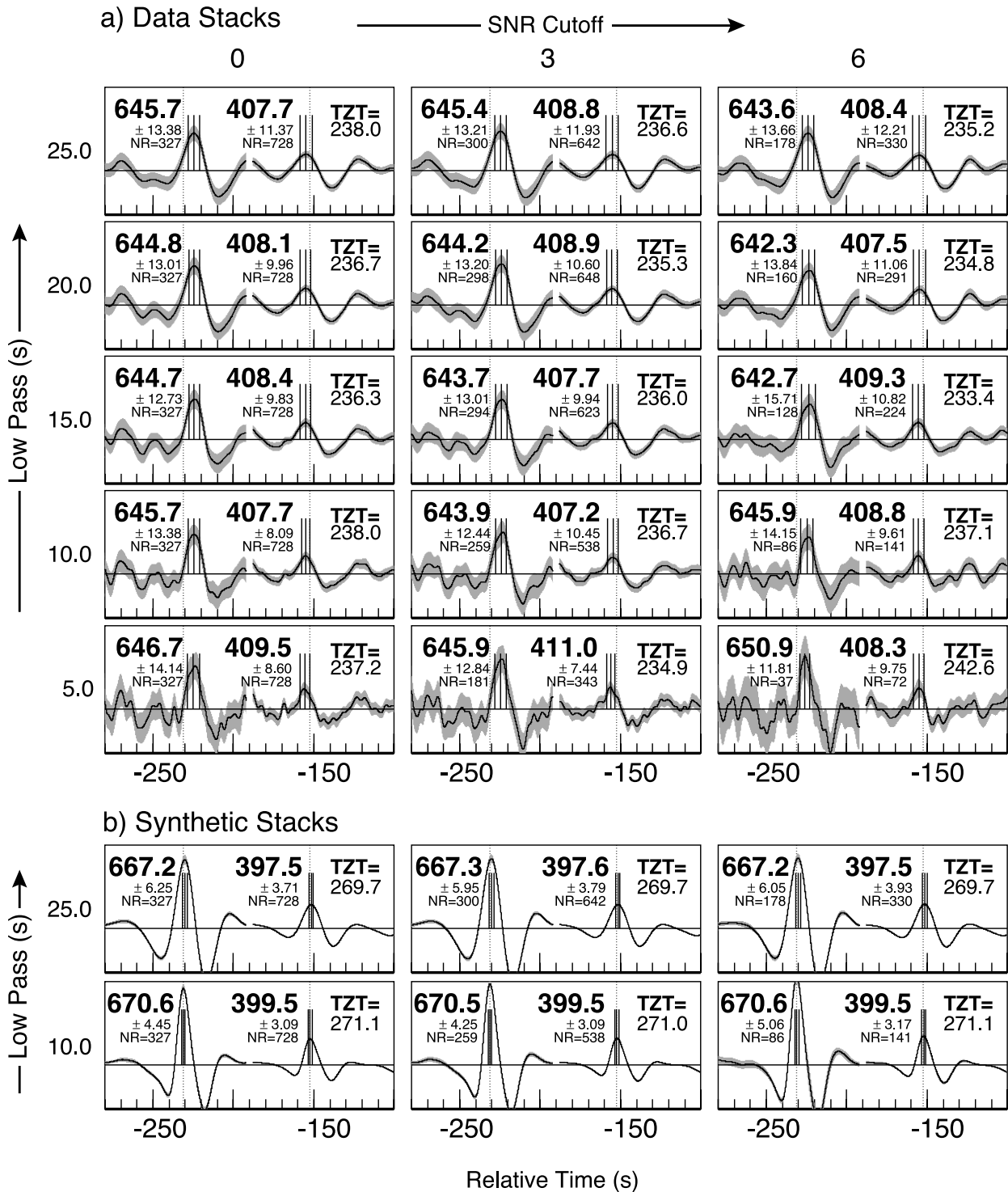


Figure 11. Example stacks on the 400 and 670 for a 10° bin located at 19.4° N and -155.3° W (the center of our study region), for (a) data and (b) the corresponding synthetics. No tomographic or crustal correction is applied to the data. The 95% confidence level from bootstrap resampling is shown in gray, with the picking bounds shown as thin lines next to the selected arrival time of each precursor. The expected PREM arrival times for S400S and S670S are shown as dotted lines. Since the 400 and 670 stacks are computed separately, the small gap at -190 s is the switch between the two different stacks. The measured discontinuity depth and number of records in each stack is shown next to the respective precursor. Records are scaled to the maximum amplitude of the SS pulse, allowing for the direct comparison of precursor amplitudes. A slight timing offset producing an offset of 2–3 km is present in the synthetics from filtering at longer periods; however, this time shift is not present in the measurement of TZ thickness, which is within 1 km of the actual value of 270 km.

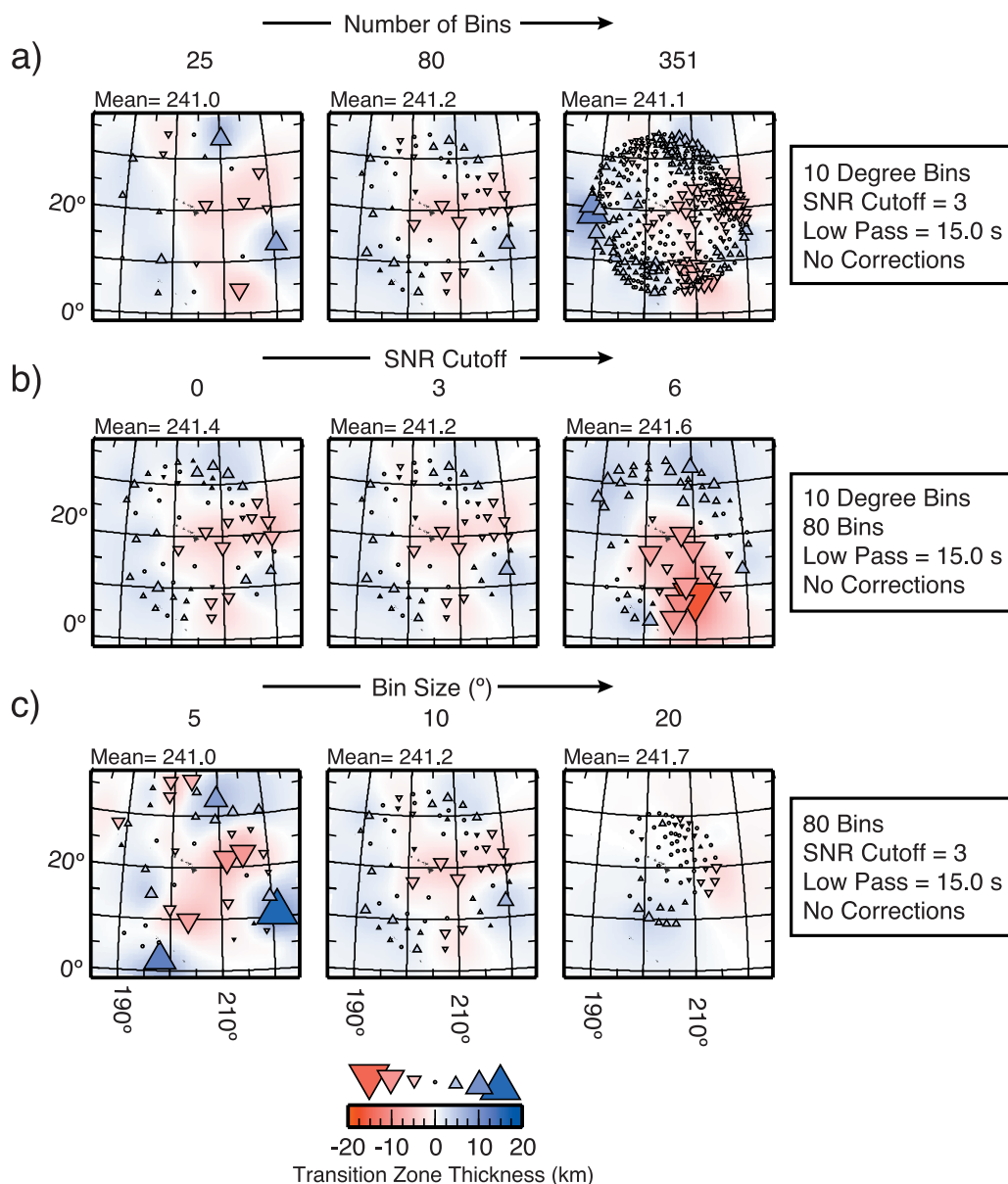


Figure 12. Experiments in bin number, SNR cutoff, and bin size. TZ thickness is plotted for each of the parameters given in the right-hand box. The measured TZ thickness for each bin is plotted as a triangle, whose size is dependent upon the amplitude of the topography relative to the mean depth. The mean topography is used as a zero line, and perturbations are plotted relative to this mean depth. A smoothed topography is plotted in the background of each panel, with red corresponding with a thinned TZ, and blue corresponding with a thickened TZ. (a) Varying number of bins. Stacks with no energy above the 95% confidence level are not plotted, resulting in 10–20% of the bins being eliminated. (b) Varying SNR cutoff values. (c) Varying bin size. See text for discussion on the differences between each set of parameters. Starting bin locations are as in Figure 8b, but the final bin locations are an average of all the bounce points falling within each bin. Since a 20° bin is the same size as our data coverage, all the bins are pushed toward the center, note that the same 80 bins are much closer to their original positions for the 5° bin size, though more stacks have been excluded.

the 670. There is a 10-km upwarping of the 670 centered on Hawaii as well as to the east of the Line Islands and a downwarping of this discontinuity in the eastern region. The 400 shows ± 6 km of relief, with a minor downwarping to the east (Figure 14a). At a SNR cutoff of 6, the pattern of relief on the 670 is relatively unchanged, but the 400

acquires much more topography, with peak-to-peak topography increasing to 19–28 km (peak-to-peak topography for the 670 is still 15–20 km), with the strongest downwarping located in the south central region, just to the east of the Line Islands. For both SNR cutoffs, the TZ appears to be thinned by 10–20 km beneath Hawaii and to the east of the

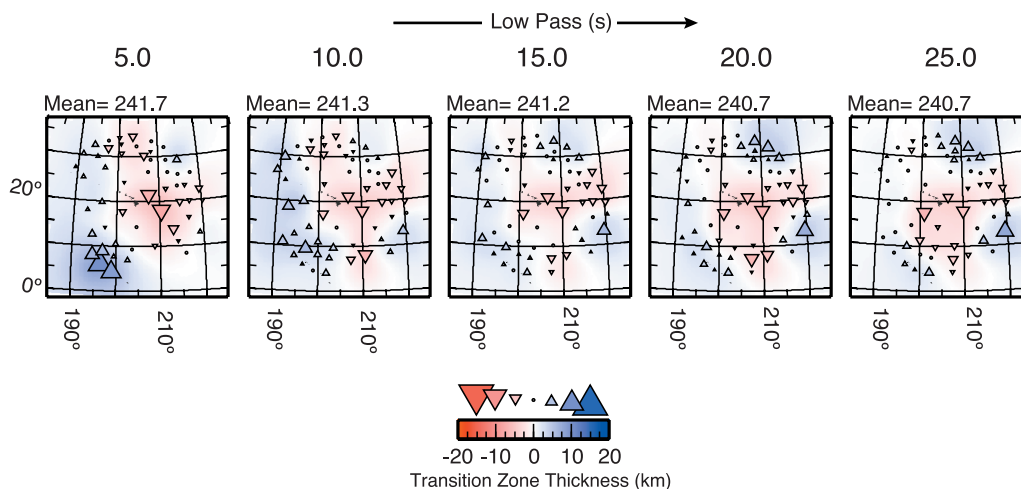


Figure 13. Geographic plot of TZ thickness as in Figure 12, except results are given for different corner frequencies for the low-pass filters of the data. No correction for upper mantle heterogeneity or crustal thickness and topography is applied. Stacking geometry is for $80^\circ 10^\circ$ bins, and the SNR cutoff is set to 3. The TZ thickness patterns are relatively insensitive to the low-pass applied to the data (see auxiliary material for the individual discontinuities), though the 5-s low-pass data show a 5-km increase in peak-to-peak variation. The number of bins excluded decreases with increasing low-pass values.

Line Islands. This regional thinning is especially pronounced in Figure 14b. It should be noted that while we only show the results for the 10-s low-pass filtered data, virtually the same pattern is found in all low passes of the data, with similar amounts of relief on each topography model (see the auxiliary material)¹.

[35] A direct comparison of our TZ thickness and discontinuity topography to other studies is complicated as each study applies different tomographic model corrections, and generally exhibit less variability through the central Pacific than in our study [e.g., *Gossler and Kind*, 1996; *Flanagan and Shearer*, 1998, 1999; *Gu and Dziewonski*, 2002; *Chambers et al.*, 2005b]. We also find a TZ thickness closer to the global average for the central Pacific; generally this region is found to have a TZ that is thinned by ~ 5 – 10 km [see *Gu and Dziewonski*, 2002, Figure 12]. However, our data set has a greatly improved sampling of the central Pacific region, and uses much shorter periods, so it is likely the differences between our topography models and those in previous studies are a result of this greater sampling density.

5.2. Discontinuity Correlation

[36] The degree of correlation between the 400 and 670 discontinuities is also investigated. Given a purely thermal origin for mantle heterogeneities, and that these anomalies extend vertically across the TZ, the 400 and 670 should be anticorrelated or negatively correlated on the basis of their Clapeyron slopes. However, upper mantle heterogeneity may not be purely thermal in origin, nor continuous across the TZ [e.g., *van Hunen et al.*, 2005], and the discontinuities may also be sensitive to compositional effects, such as large-scale compositional heterogeneity within the TZ [e.g., *Stixrude*, 1997]. By comparing the thickness of the TZ to the average velocity anomaly in the TZ, it is possible to test the Clapeyron slopes of each discontinuity.

¹Auxiliary materials are available in the HTML. doi:10.1029/2005JB004197.

[37] Figure 15 displays our imaged thicknesses of the TZ against an average TZ velocity anomaly, obtained by averaging over a 10° radius cylinder at each bin location from 450 to 600 km depth for the different tomographic models, similar to that shown in Figure 12 of *Flanagan and Shearer* [1998]. We begin the cylinder at depths offset from the actual discontinuity depths to minimize any smearing in the correction models of upper or lower mantle structure into the TZ. Also shown are several hypothetical Clapeyron slopes (see Figure 15 caption for explanation). We perform an error-weighted linear regression to find the correlation coefficient that best describes the data. Weak evidence for anticorrelated discontinuities is present in some of the models, though in general the correlation coefficients are relatively poor. The strongest correlation is seen for the SAW12D model, where the TZ thickness measurements fall along a trend consistent with the Clapeyron slopes of $+3.0$ MPa K^{-1} for the 400, and -2.0 MPa K^{-1} for the 670.

6. Discussion

6.1. Estimates of Topography Error

[38] Previous studies of the *SS* precursors report error estimates for topography in the central Pacific up to ± 10 – 15 km, we estimate our maximal topography error to be on the order of ± 5 – 15 km. This slight improvement in precision is partly the result of greater sampling in the mid-Pacific, with all stacks possessing extremely coherent energy even at short period. We estimate this error using the bootstrap boundaries (Figure 11), although the 95% confidence level does not truly represent variation in discontinuity depth, as the bootstrap error is dependent upon waveform shape and coherency. This is illustrated in Figure 11b, where we show results for synthetic stacks; the shorter-period stacks exhibit smaller error bounds by 1–2 km compared to the longer-period data, even though the background model (PREM) is the same in each synthetic.

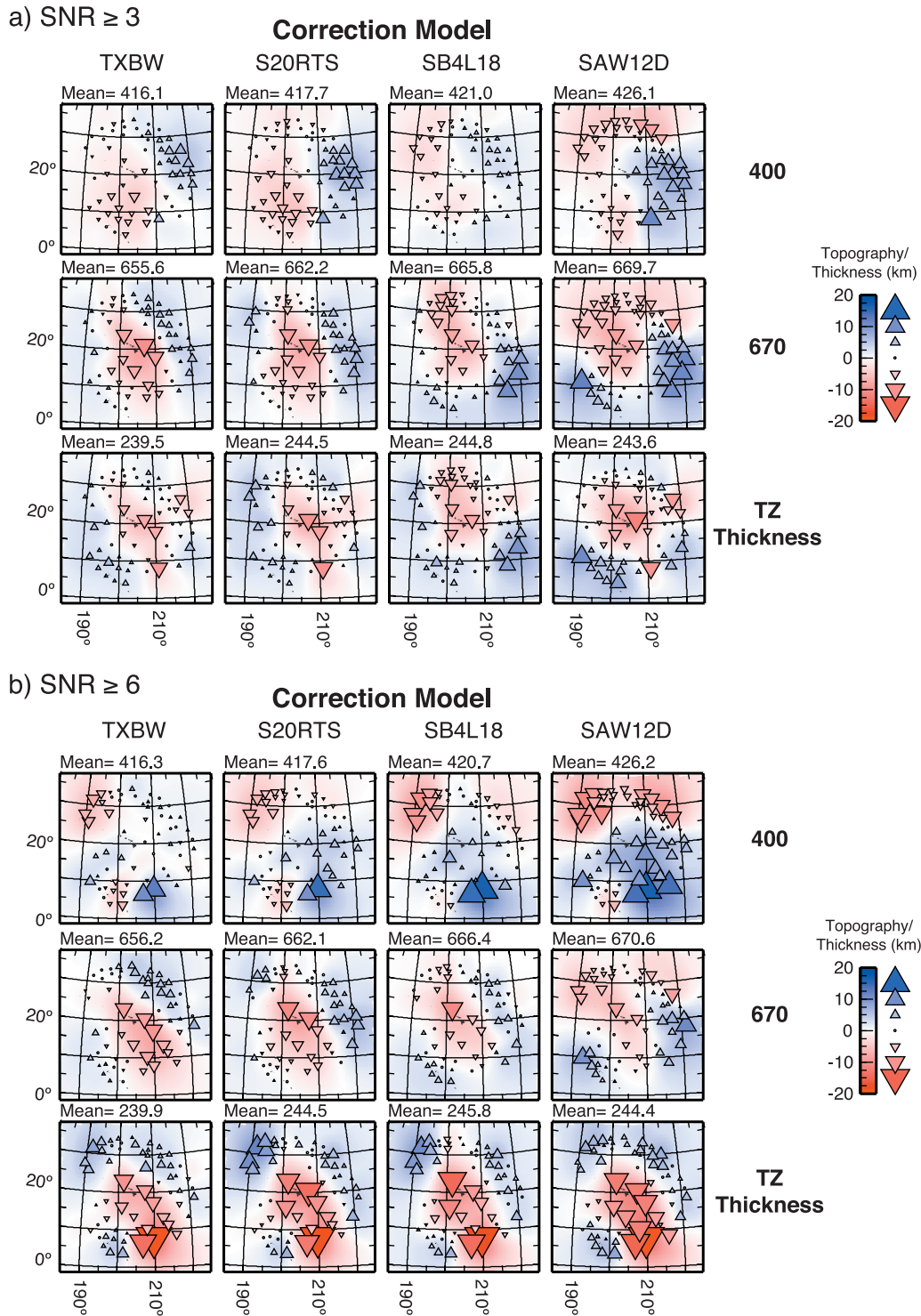


Figure 14. Geographic plot of topography as in Figure 12, the 400 and 670 discontinuities are displayed in the same way as the TZ thickness, relative to the regional mean. These results are for the 80-bin 10° radius geometry, and the low-pass filter of the stacks is 10.0 s. Each topography and thickness map is shown for the different tomographic correction models, as well as for SNR cutoffs (a) ≥ 3 and (b) ≥ 6 . Crustal thickness and topography corrections are also applied to the data. There is more relief on each discontinuity than in Figure 12, though the patterns of topography in Figure 14a resemble those in Figure 13. At higher SNR, there is much more relief on the discontinuities and TZ thickness, and the peak-to-peak topography increases in amplitude.

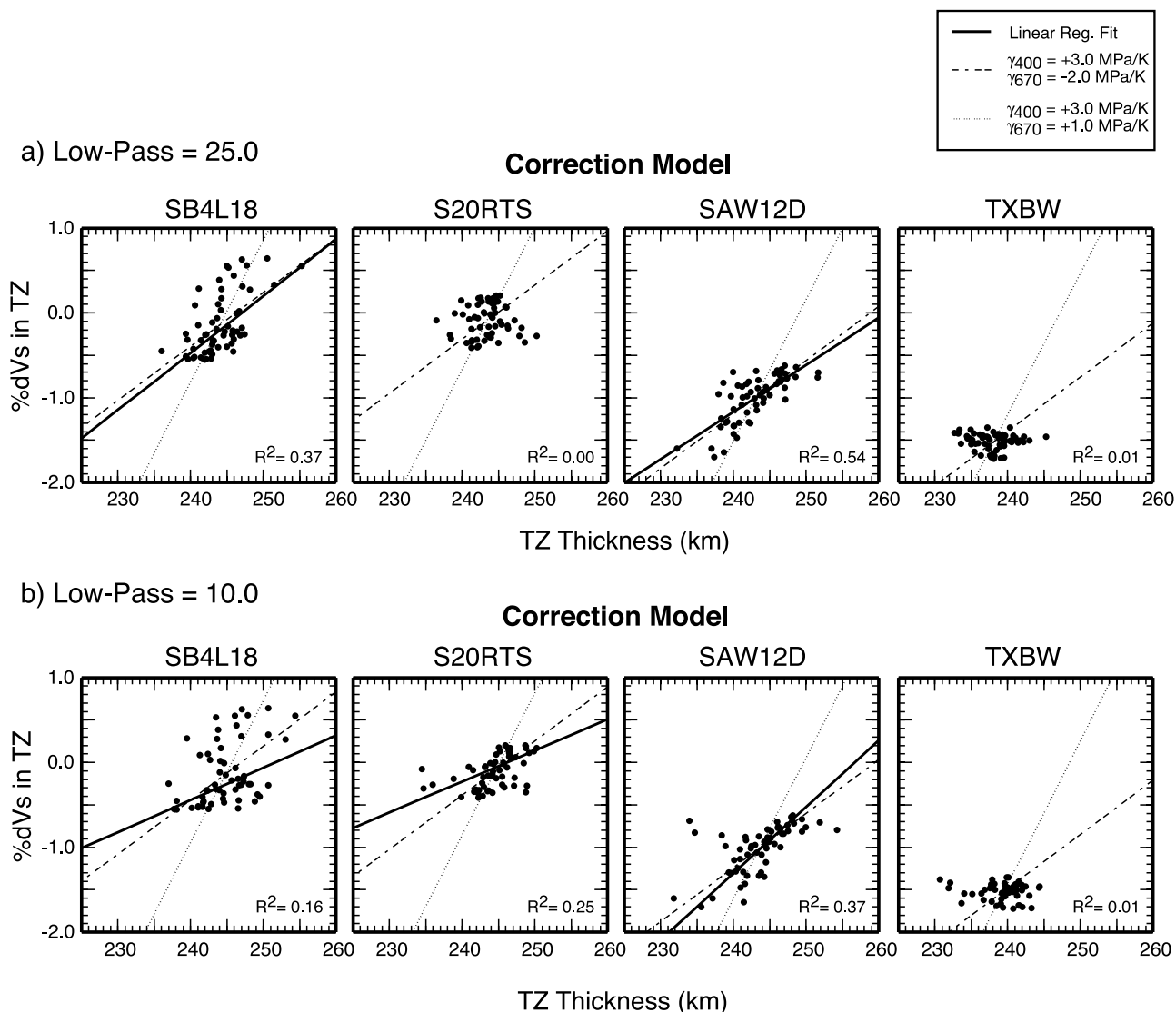


Figure 15. Plots of TZ thickness versus average velocity heterogeneity in the TZ to test for discontinuity correlation/anticorrelation for (a) 25-s low-pass filtered data and (b) 10-s low-pass filtered data. The best fitting line is found by using a weighted least squares linear regression through the data, and the R^2 correlation coefficient for each line is shown in the lower right of each plot. When the R^2 value falls close to zero, we do not plot the best fitting trend as it has no statistical significance. Several theoretical slopes are calculated using different values of the Clapeyron slopes for the 400 and 670; a value of $-4.4 \times 10^{-4} \text{ km s}^{-1} \text{ K}^{-1}$ is used for dV_s/dT^{-1} [e.g., *Revenaugh and Jordan, 1991a*], similar to the experimental results of *Jackson et al. [2005]*, who find olivine to have a dV_s/dT of -3.67×10^{-4} to $-3.84 \times 10^{-4} \text{ km s}^{-1} \text{ K}^{-1}$. These slopes are centered in each plot using the average thickness of the TZ for each correction model.

The slight offset in absolute discontinuity depth is a result of the low-pass filtering of $SdS + sSdS$, which tends to produce a small timing shift in the precursors; this offset is remedied by measuring TZ thickness. Additionally, the 670 exhibits more error than the 400 in the synthetics. This is attributed to the greater perturbation of $S670S$ amplitude over the epicentral distance range of our data; past studies have demonstrated precursor amplitude changes of several percent with increasing epicentral distance [e.g., *Shearer and Flanagan, 1999; Chambers et al., 2005a*]. We do not correct for this effect, as it does not offset measured discontinuity depth. However, this results in slightly greater bootstrap

variations in high-amplitude arrivals, as records from a range of distances are averaged together. Other sources of error (not limited to the picking error) include interfering phases, and slight offsets in discontinuity depth from inappropriate slownesses used for stacking (e.g., $S400S$ instead of $S415S$). However, on the basis of tests with PREM synthetic records, we find our error increases by 4–5 km when we do not exclude interfering phases in the synthetics, further motivating distance exclusion in the data stacks (Figure 5a). Experiments with stacking at other slownesses for a given discontinuity, such as $S400S$, $S415S$, and $S430S$, show that the picking error plus the

slight difference from the stacked slowness and actual discontinuity depth yields less than $\pm 1\text{--}2$ km uncertainty. An additional uncertainty in each stack is discontinuity depth variation within a bin, resulting in averaging precursors from variable structure. Ideally, the most prevalent depth within a bin will produce the highest and most coherent amplitude in the stack, and by picking the arrival time of this peak, we estimate the average depth of the discontinuity in the bin. However, waveform scattering effects and mantle heterogeneity may serve to defocus the precursor arrivals [see *Chaljub and Tarantola, 1997; Neele et al., 1997; Shearer et al., 1999*] and produce precursor energy over a wider set of arrival times, thus possibly perturbing the solution depth for a given bin away from the true average.

6.2. Topography and Tomographic Model Corrections

[39] The largest source of variation in our results is a consequence of the tomographic model used to correct for mantle heterogeneity. The different models produce slightly different topologies, and the base depths of the discontinuities are offset by up to 10 km, depending upon the model. The four models used in our study, SAW12D, SB4L18, S20RTS, and TXBW, use a combination of body waves and surface waves, though only SB4L18 and S20RTS use Rayleigh waves for their inversions. The SAW12D model uses longer-period data (~ 30 -s dominant period) compared to the average ~ 15 s used for the other models. In the TZ beneath our region, the SAW12D model has the largest peak-to-peak heterogeneity in the TZ (up to 1.5–2.0% in S wave velocity or V_S), while SB4L18, TXBW, and S20RTS have smaller amounts of heterogeneity ($< 1.0\%$ in V_S). The TXBW model has the highest absolute value of anomaly, but this is only after adjusting from the reference 1-D structure to the PREM reference velocity structure, otherwise the TXBW model has the smallest peak-to-peak velocity perturbations of the four correction models. The models show only moderate agreement in the TZ, and all exhibit a large degree of heterogeneity in the upper mantle (Figure 7). The S20RTS and SB4L18 models also have anomalies in the lower mantle that are near or extend across the 670, which are not present in the TXBW and SAW12D models. These differences in TZ heterogeneity propagate to the resulting topography and TZ thickness retrieved from our stacks.

[40] It is likely that the velocity heterogeneity is under accounted for in the models, both from our method for computing the correction and the underestimation of velocity heterogeneity in the models themselves [e.g., *Igel and Gudmundsson, 1997; Dahlen et al., 2000*]. The tomography corrections were applied without consideration for SS 3-D sensitivity, i.e., corrections were computed along the infinite frequency ray path. Thus an underestimation of amplitude of short-scale features in tomography models may result [*Hung et al., 2000; Zhao and Chevrot, 2003*]. Our inferred TZ thickness is also dependent on the path of the $S400S$ phase through the TZ: anomalously high (or low) velocity in the TZ results in the $S400S$ arriving earlier (or late). This travelt ime anomaly will cause the stacked phase to be mapped to a greater (shallower) depth if the high (low) velocity TZ is not accounted for by the tomographic correction. Such an unaccounted for velocity anomaly could potentially cancel out any topography present on the 400.

Likewise, an overestimate of TZ heterogeneity could amplify or introduce topographic features. A similar problem exists for unaccounted heterogeneity beneath the 670. For example, an unresolved high-velocity anomaly just below the 670 would result in a similar effect to that for the 400, either amplifying existing topography or canceling it out. The timing offset for a relatively high amount of unaccounted heterogeneity, e.g., 2%, is on the order of 1 s, which equates to approximately 3 km of discontinuity topography. This is generally far less than the possible level of topographic relief likely present in the TZ (e.g., a subduction zone). Additionally, unaccounted upper mantle heterogeneity could also be responsible for baseline shifts in the individual discontinuity topologies, we thus emphasize TZ thickness measurements, which should minimize this possible effect. Applying the tomographic corrections results in an increase in peak-to-peak TZ thickness and discontinuity topography by 2–6 km.

6.3. Possible Origins of Discontinuity Topography

[41] In previous studies, the S wave velocity structure in the TZ and the TZ thickness are found to be uncorrelated [*Gu et al., 1998*], weakly anticorrelated [e.g., *Flanagan and Shearer, 1998*], and/or anticorrelated [e.g., *Lebedev et al., 2003*]. We find evidence for a weak negative correlation of the TZ topography with the average TZ velocity anomalies (Figure 15). On the basis of the Clapeyron slopes of the discontinuities, and topography purely thermal in origin, a negative correlation would be expected, though it is possible to produce such a negative correlation when factors other than temperature are considered. A negative correlation can arise from thermal coupling across the TZ, i.e., opposite Clapeyron slopes, as well as from thermal decoupling i.e., one discontinuity experiences a thermal anomaly independent from the other, or from an anomalous TZ composition that significantly alters the Clapeyron slope of one of the discontinuities, e.g., a high proportion of garnet at the 670 [*Hirose, 2002*]. We explore several mechanisms that could produce this negative correlation.

[42] A primary geologic feature in our study region is the Hawaiian hot spot, which is a potential source of both thermal and compositional heterogeneity in the TZ. Other studies beneath the Hawaiian Islands have found the TZ to be thinned by up to 20–30 km beneath the Big Island of Hawaii, [e.g., *Li et al., 2000*], and geochemical evidence points toward a lower mantle origin of erupted material [e.g., *Lassiter and Hauri, 1998*] consistent with a continuous thermochemical anomaly upwelling through the TZ, transporting hot material from the lowermost mantle. This plume is hypothesized to have an excess temperature in the 200–300 K range, and possibly a thermal halo extending several hundred kilometers beyond the plume conduit [e.g., *Sleep, 2004*]. On the basis of the Clapeyron slopes given in Figure 15, this range of temperatures would produce an offset of 15–25 km on the 400 and 10–15 km on the 670, thus thinning the TZ by $\sim 25\text{--}40$ km. The thinnest TZ measurements in our data set (221–225 km) correspond with the locations of the Big Island of Hawaii, the best known example of a hot spot, as well as with the Line Islands. The thinning beneath Hawaii is a persistent feature across all our topography model parameters (frequency, SNR cutoffs, tomography corrections, bin geometry),

though the magnitude of thinning decreases by 5–10 km for lower SNR cutoffs, and in the uncorrected topography models. However, as shown in section 5.1, structure is smoothed in the lower SNR cutoff values, reducing the amplitude of smaller-scale detail. Also, as discussed in section 6.2, the uncorrected models are underestimates of TZ thickness; it is unlikely that the tomography models are overestimating heterogeneity in the TZ. Examination of the corresponding 400 and 670 topography in Figure 14 indicates that the majority of the thinning can be attributed to an upwarded 670, with bins located near the onset of the Hawaiian Island chain showing the largest anomalies. The 400 does not show any significant depression associated with Hawaii in Figure 14a, though in Figure 14b, the 400 beneath Hawaii is 5–10 km deeper in some correction models. As stated in section 5.1, the absolute discontinuity depths directly depend on the pattern and amplitude of upper mantle heterogeneity in the tomographic models used for time correction, which may have significant uncertainties. The TZ thickness provides a much more robust estimate, as the differential nature of the measurement minimizes any effects from upper mantle heterogeneity. Using the global mean TZ thickness of 241–242 km [Flanagan and Shearer, 1998; Gu and Dziewonski, 2002] and using our thinnest TZ measurement of 221 km, we calculate a thermal anomaly of approximately 150–180 K for 20 km of thinning. This is 5–15 km less than what would be expected for a mantle plume. The region containing the thinnest TZ would extend over very small scales (100–200 km) and would likely either be undetectable by scattering of precursor energy, or smoothed out by the large SS Fresnel zones, though the exact effects of a thinned TZ on the seismic waves requires 3-D synthetic modeling. This would imply that our TZ thickness measurement, and subsequently our inferred temperature anomaly, is an underestimate of the thermal anomaly present in the TZ. Alternatively, high-pressure experimentation with a pyrolytic mantle composition at temperatures exceeding 2100 K suggests that the ringwoodite phase decomposes to majorite at higher temperatures, resulting in a 670 arising from the majorite to perovskite phase transition [Hirose, 2002]. This phase transition is found to have a positive Clapeyron slope (+1.0 MPa K⁻¹), consequently increasing the depth of the 670 in the presence of a high-temperature anomaly. A high-temperature plume would therefore alter the expected Clapeyron slope near its center, and reduce the amount of topography expected on the discontinuities. As shown in Figure 15, this would still produce a negatively correlated relationship with TZ thickness, also supporting the hypothesis that our estimate of the thermal anomaly is a lower bound. The lateral extent of the thin TZ anomaly beneath Hawaii is ~1000 km and extends to the southeast several thousand kilometers. This is an order of magnitude larger in lateral scale than what is typically ascribed to mantle plumes (e.g., several hundred kilometers at best). While absolute topography depths are less constrained than the TZ thickness, it is interesting to note that if the 670 contains more significant topography than the 400 (as in Figure 14) then, the largest anomaly seems to be situated on this discontinuity; it is possible that the thermal structure at this depth is the result of hot material stalling at the 670, as has been suggested in several geodynamical models of plumes in the

TZ [e.g., Brunet and Yuen, 2000; Farnetani and Samuel, 2005]. Alternatively, this large-scale anomaly may be the result of scattering of seismic energy off a much smaller-scale feature, as is suggested by the modeling of [Chaljub and Tarantola, 1997; Neele et al., 1997; Neele and de Regt, 1999], though their models considered discontinuity structure in a subduction zone using a 400-km-wide trough/ridge. We plan to explore the expected wavefield effects from a plume-like feature on the discontinuities using fully 3-D synthetics in future work.

[43] Our central Pacific study region falls right on the predicted onset of reheating in the Pacific lithosphere as detailed in [Ritzwoller et al., 2004]. Ritzwoller et al. [2004] use surface waves to map the shear wave velocity in the lithosphere, and find that the apparent thermal age of the lithosphere and the measured age of the lithosphere diverge in the western Pacific. As the plate moves to the northwest, it is found to be thermally young, with the measured heat flow increasing rather than decreasing [e.g., Nagihara et al., 1996], counter to what a simple half-space cooling model would predict [e.g., Stein and Stein, 1992]. The reheating is hypothesized to be the result small-scale convection cells on the order of several hundred kilometers [van Hunen et al., 2005]. In their 3-D Cartesian model of mantle convection incorporating plate motion, van Hunen et al. [2005] find that small-scale convection delaminates lithosphere as it cools with age, this cooler material then descends into the transition zone and ultimately to the 670.

[44] Given this geodynamic model and the range of crustal ages in our region (30–120 Ma, see Figure 2c), these theoretical “drips” of cooler lithosphere are predicted to descend to at least the depth of the 400 in the western half of our region of study. As the cooler material enters the TZ, it would thermally decouple the 400 topography from that on the 670, and the 400 would become shallower with increasing crustal age. We compare the depth of the 400, and thickness of the TZ, to crustal age averaged over a 10° radius centered on each bin. Examining our topography models, we find no correlation of 400 topography or TZ thickness with crustal age, however, a pattern emerges if we only examine bins falling in crustal ages exceeding 100 Ma. We choose 100 Ma for a cutoff as the geodynamic models indicate that delaminated lithospheric material would reach the 400 by 90–100 Ma [see van Hunen et al., 2005, Figure 3c]. For our shortest period data, the shallowest 400 measurements (405–410 km) are generally associated with the oldest crustal age bins. Additionally, our thickest TZ measurements (255–260 km) also correspond with the oldest crustal age bins. The 670 is uncorrelated with crustal age in all our discontinuity topography models. For longer-period data, this correlation between the oldest crustal age with the shallowest 400 and thickest TZ measurement disappears altogether, though long period precursors to are likely less sensitive to topographic features at lateral scales of only 100–500 km, and discontinuity depths are a result of averaging over a much larger region spanning a range of ages. To use the precursors to reliably test the relationship of crustal age and discontinuity topography and subsequently the potential reheating of the lithosphere and transport of cooler material into the TZ, our coverage would have to be expanded to encompass the entire Pacific.

[45] To test these various hypotheses, fully 3-D synthetic seismograms are required in order to accurately account for the complicated *SS* wavefield sensitivity and effects of mantle heterogeneity [e.g., *Chaljub and Tarantola*, 1997; *Neele et al.*, 1997; *Neele and de Regt*, 1999; *Shearer et al.*, 1999; *Dahlen et al.*, 2000; *Hung et al.*, 2000; *Zhao and Chevrot*, 2003]. Additionally, concerns about the effect of heterogeneity on the resulting location of *SS* bounce points, as well as consideration of the actual *SS* Fresnel zone, can be explored with appropriate 3-D waveform predictions. The 3-D synthetics would be highly effectual in quantifying the trade-off between velocity heterogeneity and discontinuity topography, as well as testing the resolvability of small-scale features, such as a mantle plume or the presence of delaminated lithosphere entering into the TZ. This is especially relevant for shorter periods, e.g., 5–10 s, and is left for future work.

7. Conclusions

[46] We have presented new topography models for the 400- and 670-km discontinuities, as well as TZ thickness measurements, beneath the central Pacific using an *SS* precursor data set that vastly improves sampling in this region. We do not robustly detect discontinuities other than the 400 and 670; we do find weak returns from the 220 and 520, though the amplitudes of these discontinuities are not well developed above the 95% confidence level. We find topography to be primarily dependent on the quality of the data used, and also on the tomographic correction applied for mantle heterogeneity, but do not find strong evidence for an increase in peak-to-peak topography with shorter periods. The average TZ thickness beneath our central Pacific region is approximately 242 ± 3 km, in good agreement with past global precursor studies. A weak negative correlation exists between the TZ thickness and TZ heterogeneity, with a 10–20 km thinning of the TZ present beneath the Hawaiian hot spot and also to the southeast beneath the Line Islands. Ascribing this thinning completely to thermal effects indicates a minimum of 100–200 K excess temperature anomaly in the TZ. Additionally, we find the thickest TZ measurements in our study region correspond to the oldest crustal ages, and that the 400 is elevated beneath these bins. This is consistent with colder lithosphere delaminated from small-scale convection in the upper mantle entering the TZ and elevating the 400-km discontinuity.

[47] **Acknowledgments.** We thank Allen McNamara, Sebastian Rost, Michael Thorne, and Lars Stixrude for numerous useful discussions. We also thank *Wessel and Smith* [1998] for their Generic Mapping Tools package, which was used to draft most of the figures in this manuscript. This paper made use of the TauP Toolkit, developed by *Crotwell et al.* [1999]. Data used in this study came from IRIS, GEOSCOPE, GEOFON, and the CNSN; we would like to thank them for making data publicly available. We also thank the Scripps, Caltech, Berkeley, and Texas groups for making their topography models available for download. We are indebted to Don Forsyth, Peter Shearer, and Yu Jeffrey Gu, whose comments greatly improved the manuscript. N.S. was supported in this research by a NSF Graduate Research Fellowship. E.G. was partially supported by NSF grant EAR-0135119.

References

Anderson, D. L. (2005), Scoring hotspots: The plume and plate paradigms, in *Plates, Plumes, and Paradigms*, edited by G. R. Foulger et al., *Geol. Soc. Am. Spec. Pap.*, 388, 31–54.

- Bassin, C., G. Laske, and G. Masters (2000), The current limits of resolution for surface wave tomography in North America, *Eos Trans AGU*, 81(48), Fall Meet. Suppl., Abstract S12A-03.
- Bina, C. R., and G. Helffrich (1994), Phase-transition Clapeyron slopes and transition zone seismic discontinuity topography, *J. Geophys. Res.*, 99(B8), 15,853–15,860.
- Brunet, D., and D. A. Yuen (2000), Mantle plumes pinched in the transition zone, *Earth Planet. Sci. Lett.*, 178(1–2), 13–27.
- Chaljub, E., and A. Tarantola (1997), Sensitivity of *SS* precursors to topography on the upper-mantle 660-km discontinuity, *Geophys. Res. Lett.*, 24(21), 2613–2616.
- Chambers, K., A. Deuss, and J. H. Woodhouse (2005a), Reflectivity of the 410–km discontinuity from *PP* and *SS* precursors, *J. Geophys. Res.*, 110, B02301, doi:10.1029/2004JB003345.
- Chambers, K., J. H. Woodhouse, and A. Deuss (2005b), Topography of the 410–km discontinuity from *PP* and *SS* precursors, *Earth Planet. Sci. Lett.*, 235(3–4), 610–622.
- Chevrot, S., L. Vinnik, and J. P. Montagner (1999), Global-scale analysis of the mantle Pds phases, *J. Geophys. Res.*, 104(B9), 20,203–20,219.
- Choy, G. L., and P. G. Richards (1975), Pulse distortion and Hilbert transformation in multiply reflected and refracted body waves, *Bull. Seismol. Soc. Am.*, 65(1), 55–70.
- Crotwell, H. P., T. J. Owens, and J. Ritsema (1999), The TauP toolkit: Flexible seismic travel-time and ray-path utilities, *Seismol. Res. Lett.*, 70, 154–160.
- Cserepes, L., U. R. Christensen, and N. M. Ribe (2000), Geoid height versus topography for a plume model of the Hawaiian swell, *Earth Planet. Sci. Lett.*, 178(1–2), 29–38.
- Dahlen, F. A., S. H. Hung, and G. Nolet (2000), Frechet kernels for finite-frequency traveltimes - I. Theory, *Geophys. J. Int.*, 141(1), 157–174.
- Deuss, A., and J. Woodhouse (2001), Seismic observations of splitting of the mid-transition zone discontinuity in Earth's mantle, *Science*, 294(5541), 354–357.
- Deuss, A., and J. H. Woodhouse (2002), A systematic search for mantle discontinuities using *SS*-precursors, *Geophys. Res. Lett.*, 29(8), 1249, doi:10.1029/2002GL014768.
- Dziewonski, A. M., and D. L. Anderson (1981), Preliminary Reference Earth Model, *Phys. Earth Planet. Inter.*, 25(4), 297–356.
- Efron, B., and R. Tibshirani (1986), Bootstrap methods for standard errors, confidence intervals, and other measures of statistical accuracy, *Stat. Sci.*, 1(1), 54–75.
- Farnetani, C. G., and H. Samuel (2005), Beyond the thermal plume paradigm, *Geophys. Res. Lett.*, 32, L07311, doi:10.1029/2005GL022360.
- Flanagan, M. P., and P. M. Shearer (1998), Global mapping of topography on transition zone velocity discontinuities by stacking *SS* precursors, *J. Geophys. Res.*, 103(B2), 2673–2692.
- Flanagan, M. P., and P. M. Shearer (1999), A map of topography on the 410–km discontinuity from *PP* precursors, *Geophys. Res. Lett.*, 26(5), 549–552.
- Fuchs, K., and G. Müller (1971), Computation of synthetic seismograms with the reflectivity method and comparison with observations, *Geophys. J. R. Astron. Soc.*, 23, 417–433.
- Gossler, J., and R. Kind (1996), Seismic evidence for very deep roots of continents, *Earth Planet. Sci. Lett.*, 138(1–4), 1–13.
- Grand, S. P. (2002), Mantle shear-wave tomography and the fate of subducted slabs, *Philos. Trans. R. Soc. London, Ser. A*, 360(1800), 2475–2491.
- Grand, S. P., and D. V. Helmberger (1984), Upper mantle shear structure of North-America, *Geophys. J. R. Astron. Soc.*, 76(2), 399–438.
- Gu, Y. J., and A. M. Dziewonski (2002), Global variability of transition zone thickness, *J. Geophys. Res.*, 107(B7), 2135, doi:10.1029/2001JB000489.
- Gu, Y., A. M. Dziewonski, and C. B. Agee (1998), Global de-correlation of the topography of transition zone discontinuities, *Earth Planet. Sci. Lett.*, 157(1–2), 57–67.
- Gu, Y. J., A. M. Dziewonski, and G. Ekstrom (2001), Preferential detection of the Lehmann discontinuity beneath continents, *Geophys. Res. Lett.*, 28(24), 4655–4658.
- Gu, Y. J., A. M. Dziewonski, and G. Ekstrom (2003), Simultaneous inversion for mantle shear velocity and topography of transition zone discontinuities, *Geophys. J. Int.*, 154(2), 559–583.
- Helffrich, G. (2000), Topography of the transition zone seismic discontinuities, *Rev. Geophys.*, 38(1), 141–158.
- Hilton, D. R., G. M. McMurtry, and R. Kreulen (1997), Evidence for extensive degassing of the Hawaiian mantle plume from helium-carbon relationships at Kilauea volcano, *Geophys. Res. Lett.*, 24(23), 3065–3068.
- Hirose, K. (2002), Phase transitions in pyrolitic mantle around 670-km depth: Implications for upwelling of plumes from the lower mantle, *J. Geophys. Res.*, 107(B4), 2078, doi:10.1029/2001JB000597.

- Hung, S. H., F. A. Dahlen, and G. Nolet (2000), Frechet kernels for finite-frequency traveltimes - II. Examples, *Geophys. J. Int.*, *141*(1), 175–203.
- Igel, H., and O. Gudmundsson (1997), Frequency-dependent effects on travel times and waveforms of long-period *S* and *SS* waves, *Phys. Earth Planet. Inter.*, *104*(1–3), 229–246.
- Ito, E., and E. Takahashi (1989), Postspinel transformations in the system Mg_2SiO_4 – Fe_2SiO_4 and some geophysical implications, *J. Geophys. Res.*, *94*(B8), 10,637–10,646.
- Jackson, I., S. Webb, L. Weston, and D. Boness (2005), Frequency dependence of elastic wave speeds at high temperature: A direct experimental demonstration, *Phys. Earth Planet. Inter.*, *148*(1), 85–96.
- Jordan, T. H. (1975), Continental tectosphere, *Rev. Geophys.*, *13*(3), 1–12.
- Karato, S. (1992), On the Lehmann discontinuity, *Geophys. Res. Lett.*, *19*(22), 2255–2258.
- Katsura, T., and E. Ito (1989), The system Mg_2SiO_4 – Fe_2SiO_4 at high-pressures and temperatures: Precise determination of stabilities of olivine, modified spinel, and spinel, *J. Geophys. Res.*, *94*(B11), 15,663–15,670.
- Lassiter, J. C., and E. H. Hauri (1998), Osmium-isotope variations in Hawaiian lavas: Evidence for recycled oceanic lithosphere in the Hawaiian plume, *Earth Planet. Sci. Lett.*, *164*(3–4), 483–496.
- Lebedev, S., S. Chevrot, and R. D. van der Hilst (2003), Correlation between the shear-speed structure and thickness of the mantle transition zone, *Phys. Earth Planet. Inter.*, *136*(1–2), 25–40.
- Lee, D. K., and S. P. Grand (1996), Depth of the upper mantle discontinuities beneath the East Pacific Rise, *Geophys. Res. Lett.*, *23*(23), 3369–3372.
- Lehmann, I. (1961), *S* and the structure of the upper mantle, *Geophys. J. R. Astron. Soc.*, *4*, 124–138.
- Lei, J. S., and D. P. Zhao (2006), A new insight into the Hawaiian plume, *Earth Planet. Sci. Lett.*, *241*(3–4), 438–453.
- Li, X., R. Kind, K. Priestley, S. V. Sobolev, F. Tilmann, X. Yuan, and M. Weber (2000), Mapping the Hawaiian plume conduit with converted seismic waves, *Nature*, *405*(6789), 938–941.
- Li, X. D., and B. Romanowicz (1996), Global mantle shear velocity model developed using nonlinear asymptotic coupling theory, *J. Geophys. Res.*, *101*(B10), 22,245–22,272.
- Li, X. Q., R. Kind, X. H. Yuan, I. Wolbern, and W. Hanka (2004), Rejuvenation of the lithosphere by the Hawaiian plume, *Nature*, *427*(6977), 827–829.
- Liu, M., and C. G. Chase (1991), Evolution of Hawaiian basalts: A hotspot melting model, *Earth Planet. Sci. Lett.*, *104*(2–4), 151–165.
- Masters, G., G. Laske, H. Bolton, and A. M. Dziewonski (2000), The relative behavior of shear velocity, bulk sound speed, and compressional velocity in the mantle: Implications for chemical and thermal structure, in *Earth's Deep Interior: Mineral Physics and Tomography From the Atomic to the Global Scale*, *Geophys. Monogr. Ser.*, vol. 117, edited by S. Karato et al., pp. 63–87, AGU, Washington, D. C.
- Montelli, R., G. Nolet, F. A. Dahlen, G. Masters, E. R. Engdahl, and S. H. Hung (2004), Finite-frequency tomography reveals a variety of plumes in the mantle, *Science*, *303*(5656), 338–343.
- Moore, W. B., G. Schubert, and P. Tackley (1998), Three-dimensional simulations of plume-lithosphere interaction at the Hawaiian swell, *Science*, *279*(5353), 1008–1011.
- Morgan, W. J. (1972), Deep mantle convection plumes and plate motions, *Am. Assoc. Pet. Geol. Bull.*, *56*(2), 203–213.
- Müller, G. (1985), The reflectivity method: A tutorial, *J. Geophys.*, *58*, 153–174.
- Müller, R. D., W. R. Roest, J. Y. Royer, L. M. Gahagan, and J. G. Sclater (1997), Digital isochrons of the world's ocean floor, *J. Geophys. Res.*, *102*(B2), 3211–3214.
- Nagihara, S., C. R. B. Lister, and J. G. Sclater (1996), Reheating of old oceanic lithosphere: Deductions from observations, *Earth Planet. Sci. Lett.*, *139*(1–2), 91–104.
- Neele, F., and H. deRegt (1999), Imaging upper-mantle discontinuity topography using underside-reflection data, *Geophys. J. Int.*, *137*(1), 91–106.
- Neele, F., and R. Snieder (1992), Topography of the 400-km discontinuity from observations of long-period P400p phases, *Geophys. J. Int.*, *109*(3), 670–682.
- Neele, F., H. deRegt, and J. VanDecar (1997), Gross errors in upper-mantle discontinuity topography from underside reflection data, *Geophys. J. Int.*, *129*(1), 194–204.
- Niu, F. L., H. Inoue, D. Suetsugu, and K. Kanjo (2000), Seismic evidence for a thinner mantle transition zone beneath the South Pacific Superswell, *Geophys. Res. Lett.*, *27*(13), 1981–1984.
- Niu, F. L., S. C. Solomon, P. G. Silver, D. Suetsugu, and H. Inoue (2002), Mantle transition-zone structure beneath the South Pacific Superswell and evidence for a mantle plume underlying the Society hotspot, *Earth Planet. Sci. Lett.*, *198*(3–4), 371–380.
- Revenaugh, J., and T. H. Jordan (1991a), Mantle layering from *ScS* reverberations: 2. The transition zone, *J. Geophys. Res.*, *96*(B12), 19,763–19,780.
- Revenaugh, J., and T. H. Jordan (1991b), Mantle layering from *ScS* reverberations: 3. The upper mantle, *J. Geophys. Res.*, *96*(B12), 19,781–19,810.
- Ribe, N. M. (1988), Dynamical geochemistry of the Hawaiian plume, *Earth Planet. Sci. Lett.*, *88*(1–2), 37–46.
- Richards, M. A., and C. Lithgow-Bertelloni (1996), Plate motion changes, the Hawaiian-Emperor Bend, and the apparent success and failure of geodynamic models, *Earth Planet. Sci. Lett.*, *137*(1–4), 19–27.
- Ringwood, A. E. (1975), *Composition and Petrology of the Earth's Interior*, 618 pp., McGraw-Hill, New York.
- Ritsema, J., H. J. van Heijst, and J. H. Woodhouse (1999), Complex shear wave velocity structure imaged beneath Africa and Iceland, *Science*, *286*(5446), 1925–1928.
- Ritzwoller, M. H., N. M. Shapiro, and S. J. Zhong (2004), Cooling history of the Pacific lithosphere, *Earth Planet. Sci. Lett.*, *226*(1–2), 69–84.
- Rost, S., and M. Weber (2002), The upper mantle transition zone discontinuities in the Pacific as determined by short-period array data, *Earth Planet. Sci. Lett.*, *204*(3–4), 347–361.
- Ryberg, T., F. Wenzel, A. V. Egorkin, and L. Solodilov (1998), Properties of the mantle transition zone in northern Eurasia, *J. Geophys. Res.*, *103*(B1), 811–822.
- Shearer, P. M. (1990), Seismic imaging of upper-mantle structure with new evidence for a 520-km discontinuity, *Nature*, *344*(6262), 121–126.
- Shearer, P. M. (1991), Imaging global body wave phases by stacking long-period seismograms, *J. Geophys. Res.*, *96*(B12), 20,353–20,364.
- Shearer, P. M. (1993), Global mapping of upper-mantle reflectors from long-period *SS* precursors, *Geophys. J. Int.*, *115*(3), 878–904.
- Shearer, P. M. (1996), Transition zone velocity gradients and the 520-km discontinuity, *J. Geophys. Res.*, *101*(B2), 3053–3066.
- Shearer, P. M. (2000), Upper mantle discontinuities, in *Earth's Deep Interior: Mineral Physics and Tomography From the Atomic to the Global Scale*, *Geophys. Monogr. Ser.*, vol. 117, edited by S. Karato et al., pp. 115–131, AGU, Washington, D. C.
- Shearer, P. M., and M. P. Flanagan (1999), Seismic velocity and density jumps across the 410- and 660-kilometer discontinuities, *Science*, *285*(5433), 1545–1548.
- Shearer, P. M., and T. G. Masters (1992), Global mapping of topography on the 660-km discontinuity, *Nature*, *355*(6363), 791–796.
- Shearer, P. M., M. P. Flanagan, and M. A. H. Hedlin (1999), Experiments in migration processing of *SS* precursor data to image upper mantle discontinuity structure, *J. Geophys. Res.*, *104*(B4), 7229–7242.
- Sleep, N. H. (1990), Hotspots and mantle plumes: Some phenomenology, *J. Geophys. Res.*, *95*(B5), 6715–6736.
- Sleep, N. H. (2004), Thermal haloes around plume tails, *Geophys. J. Int.*, *156*(2), 359–362.
- Song, T. R. A., D. V. Helmberger, and S. P. Grand (2004), Low-velocity zone atop the 410-km seismic discontinuity in the northwestern United States, *Nature*, *427*(6974), 530–533.
- Stein, C. A., and S. Stein (1992), A model for the global variation in oceanic depth and heat-flow with lithospheric age, *Nature*, *359*(6391), 123–129.
- Steinberger, B. (2000), Plumes in a convecting mantle: Models and observations for individual hotspots, *J. Geophys. Res.*, *105*(B5), 11,127–11,152.
- Stixrude, L. (1997), Structure and sharpness of phase transitions and mantle discontinuities, *J. Geophys. Res.*, *102*(B7), 14,835–14,852.
- van Hunen, J., S. J. Zhong, N. M. Shapiro, and M. H. Ritzwoller (2005), New evidence for dislocation creep from 3-D geodynamic modeling of the Pacific upper mantle structure, *Earth Planet. Sci. Lett.*, *238*, 146–155.
- Wessel, P., and W. H. F. Smith (1998), New, improved version of Generic Mapping Tools released, *Eos Trans AGU*, *79*(47), 579.
- Williams, Q., and J. Revenaugh (2005), Ancient subduction, mantle eclogite, and the 300 km seismic discontinuity, *Geology*, *33*(1), 1–4.
- Woodland, A. B. (1998), The orthorhombic to high-P monoclinic phase transition in Mg-Fe pyroxenes: Can it produce a seismic discontinuity?, *Geophys. Res. Lett.*, *25*(8), 1241–1244.
- Zhao, L., and S. Chevrot (2003), *SS*-wave sensitivity to upper mantle structure: Implications for the mapping of transition zone discontinuity topographies, *Geophys. Res. Lett.*, *30*(11), 1590, doi:10.1029/2003GL017223.
- Zhong, S. J., and A. B. Watts (2002), Constraints on the dynamics of mantle plumes from uplift of the Hawaiian Islands, *Earth Planet. Sci. Lett.*, *203*(1), 105–116.

E. Garnero and N. Schmerr, Department of Geological Sciences, Arizona State University, Box 871404, Tempe, AZ 85287-1404, USA. (nsmchmer@asu.edu)